



HAL
open science

The intra-seasonal dynamics of the mixed layer pump in the subpolar North Atlantic Ocean: a BGC-Argo float approach

L. Lacour, N. Briggs, Hervé Claustre, M. Ardyna, G. Dall’Olmo

► **To cite this version:**

L. Lacour, N. Briggs, Hervé Claustre, M. Ardyna, G. Dall’Olmo. The intra-seasonal dynamics of the mixed layer pump in the subpolar North Atlantic Ocean: a BGC-Argo float approach. *Global Biogeochemical Cycles*, 2019, 33 (3), pp.266-281. 10.1029/2018GB005997 . hal-02337414

HAL Id: hal-02337414

<https://hal.sorbonne-universite.fr/hal-02337414v1>

Submitted on 29 Oct 2019

HAL is a multi-disciplinary open access archive for the deposit and dissemination of scientific research documents, whether they are published or not. The documents may come from teaching and research institutions in France or abroad, or from public or private research centers.

L’archive ouverte pluridisciplinaire **HAL**, est destinée au dépôt et à la diffusion de documents scientifiques de niveau recherche, publiés ou non, émanant des établissements d’enseignement et de recherche français ou étrangers, des laboratoires publics ou privés.

The intra-seasonal dynamics of the mixed layer pump in the subpolar North Atlantic Ocean: a BGC-Argo float approach.

L. Lacour^{1†}, N. Briggs², H. Claustre¹, M. Ardyna^{1,3}, G. Dall’Olmo^{4,5}

¹Sorbonne Université, CNRS, Laboratoire d’Océanographie de Villefranche, LOV, F-06230 Villefranche-sur-mer, France.

²National Oceanography Centre, European Way, Southampton SO14 3ZH, UK.

³Department of Earth System Science, Stanford University, Stanford CA 94305, USA.

⁴Plymouth Marine Laboratory, Prospect Place, The Hoe, Plymouth PL1 3DH, UK.

⁵National Centre for Earth Observation, Plymouth Marine Laboratory, Prospect Place, The Hoe, Plymouth PL1 3DH, UK.

Corresponding author: Léo Lacour (leo.lacour@takuvik.ulaval.ca)

† Now at Takuvik Joint International Laboratory, CNRS and Université Laval, Québec, G1V0A6, Canada.

Key Points:

- The density of BGC-Argo float network enables identification of episodic mixed layer pump events on a basin-scale.
- Intra-seasonal dynamics of the mixed layer pump drives episodic inputs of fresh organic material to the mesopelagic during the winter to spring transition.
- This mechanism provides a significant source of energy to the mesopelagic food-web before the spring bloom period.

Abstract

The detrainment of organic matter from the mixed layer, a process known as the mixed layer pump (ML pump), has long been overlooked in carbon export budgets. Recently, the ML pump has been investigated at seasonal scale and appeared to contribute significantly to particulate organic carbon export to the mesopelagic zone, especially at high latitudes where seasonal variations of the mixed layer depth are large. However, the dynamics of the ML pump at intra-seasonal scales remains poorly known, mainly because the lack of observational tools suited to

33 studying such dynamics. In the present study, using a dense network of autonomous profiling
34 floats equipped with bio-optical sensors, we captured widespread episodic ML pump-driven
35 export events, during the winter and early spring period, in a large part of the subpolar North
36 Atlantic Ocean. The intra-seasonal dynamic of the ML pump exports fresh organic material to
37 depth (basin-scale average up to $55 \text{ mg C m}^{-2} \text{ d}^{-1}$), providing a significant source of energy to
38 the mesopelagic food web before the spring bloom period. This mechanism may sustain the
39 seasonal development of overwintering organisms such as copepods with potential impact on
40 the characteristics of the forthcoming spring phytoplankton bloom through predator-prey
41 interactions.

42

43 **1 Introduction**

44 The export of organic matter from the surface to the ocean interior has traditionally been
45 attributed to the gravitational settling of particulate organic carbon (POC), namely the
46 biological gravitational pump (Sanders et al., 2014; Siegel et al., 2016). The gravitational pump
47 at high latitudes is closely related to the spring phytoplankton bloom (Martin et al., 2011). Large
48 phytoplankton cells such as diatoms ($> 20 \mu\text{m}$) that thrive during the spring bloom contribute
49 significantly to the downward carbon flux due to their high sinking rate (up to 50 m d^{-1} , Villa-
50 Alfageme et al., 2016), and their ability to form large aggregates (Smetacek, 1985, 1999).
51 Zooplankton also play a key role by repackaging organic matter into fecal pellets, thereby
52 enhancing the speed at which it sinks out of the euphotic zone (Turner, 2002, 2015). Up to 90%
53 of the exported material may be consumed and remineralized back into dissolved inorganic
54 carbon (DIC) by heterotrophic activity in the mesopelagic zone ($\sim 100 - 1,000 \text{ m}$; Buesseler &
55 Boyd, 2009; Kwon et al., 2009). Finally, a small fraction of this material may be sequestered in
56 the bathypelagic zone ($> 1,000 \text{ m}$) on timescales of months to millennia (Ducklow et al., 2001;
57 Poulton et al., 2006).

58 In complement to the biological gravitational pump, Lévy et al. (2001), Omand et al. (2015)
59 and Llorca et al. (2018) provided evidence that export of organic matter also occurs through
60 localized (1-10 km) eddy-driven subduction of non-sinking particles, and possibly dissolved
61 organic carbon (DOC). In subpolar oceans, the eddy-driven subduction pump may contribute
62 up to half of the total springtime export of POC (Omand et al., 2015). Through eddy-driven
63 stratification, these submesoscale processes can also enhance the production of organic matter
64 at the surface which will potentially be exported by subsequent eddy-driven subduction
65 (Mahadevan et al., 2012; Omand et al., 2015). Submesoscale subduction thus leads to episodic
66 injections of POC- and DOC-rich waters below the mixed layer, possibly outside the spring

67 bloom period. As current estimates of metabolic activity in the mesopelagic region exceed the
68 influx of organic substrates generally attributed to the biological pump (Burd et al., 2010;
69 Giering et al., 2014; Steinberg et al., 2008), submesoscale subduction has been invoked as an
70 alternate pathway allowing a better balance of the carbon budget (Barth et al., 2002; Lévy et
71 al., 2001; Omand et al., 2015). The spatial heterogeneity of this process could indeed stimulate
72 hotspots of organic substrates, likely missed by conventional sampling methods.

73 Recently, Dall’Olmo et al. (2016) highlighted the global impact on carbon export budgets of
74 seasonal detrainment of organic matter, a process known as the seasonal mixed layer pump (ML
75 pump). A few localized studies had first described this mechanism at the diurnal timescale,
76 showing that alternation of night convection and daily restratification can lead to an
77 entrainment-detrainment cycle of particles from the mixed layer (Gardner et al., 1995; Ho &
78 Marra, 1994; Woods & Onken, 1982). Indeed, the mixed layer deepens due to the effect of wind
79 and heat loss to the atmosphere (Price et al., 1986) but does not shoal smoothly, as commonly
80 assumed for the sake of simplicity. Instead, the upper-ocean stratifies due to solar heating or
81 other sources (e.g. freshwater flux, slumping of isopycnals) and eventually a new mixed layer
82 re-forms from the surface, thereby isolating phytoplankton cells and other particles in the so-
83 called remnant layer (Franks, 2015; Ho & Marra, 1994; Fig. 1). At the diurnal timescale, the
84 amplitude of the mixing layer depth variation is small (Woods & Onken, 1982) and much of
85 the detrained organic material can be entrained back into the mixing layer. Thereby, the net
86 export of carbon by the ML pump is accordingly weak. At the seasonal scale, however, the ML
87 pump is a process of greater significance (Carlson et al., 1994; Dall’Olmo et al., 2016;
88 Dall’Olmo & Mork, 2014). In springtime, the seasonal stratification of deep mixed layers
89 contributes to export large amounts of carbon as dissolved organic matter or small non-sinking
90 particles. In high-latitude regions with deep winter mixing, the seasonal ML pump amounts on
91 average to 23% of the carbon supplied by fast sinking particles (Dall’Olmo et al., 2016).

92 The winter to spring evolution of the mixed layer depth (MLD) does not correspond to a smooth
93 shoaling but rather is interspersed with restratification and deep mixing events (Lacour et al.,
94 2017). Such intermittent mixing can enhance both phytoplankton production and POC export
95 through the so-called intra-seasonal ML pump (Bishop et al., 1986; Garside & Garside, 1993;
96 Giering et al., 2016; Koeve et al., 2002). When detrainment fluxes exceed entrainment fluxes,
97 the intra-seasonal ML pump can lead to a net export of carbon to the mesopelagic. In the north-
98 east Iceland basin, Giering et al. (2016) have shown that the pre-bloom flux of small particles
99 driven by the ML pump can be of similar magnitude to the total particle export rate by
100 sedimentation observed during, and after, the spring bloom period. However, the analysis of

101 long-term sediment trap data from 3000 m at the Porcupine Abyssal Plain (49°N, 16°W)
102 revealed that pre-bloom deep fluxes are small (Lampitt et al., 2010). This discrepancy suggests
103 that most of the particulate material exported by the ML pump is consumed in the mesopelagic
104 zone (Giering et al., 2016), and potentially ventilated back into the atmosphere the following
105 winter as inorganic carbon. Thus, this process may be less relevant to the long-term
106 sequestration of carbon than for supplying energy to the mesopelagic food-web. In particular,
107 zooplankton populations, especially overwintering organisms, inhabiting cold, dark and low
108 turbulence environments at depth (Jónasdóttir et al., 2015; Steinberg & Landry, 2017; Visser et
109 al., 2001) could benefit from the ML pump.

110 These three main pathways of carbon (i.e. the gravitational pump, the eddy-driven pump and
111 the mixed layer pump) all contribute to the biological carbon pump (Dall’Olmo et al., 2016;
112 Siegel et al., 2016; Llort et al., 2018). Indeed, they transfer organic matter from the productive
113 mixing layer to the ocean interior where light and mixing are reduced. The amount of exported
114 material determines the strength of the biological pump while the sequestration timescale
115 control its efficiency (Buesseler & Boyd, 2009). For the particular case of the intra-seasonal
116 ML pump, the strength is defined as the net amount of particulate organic carbon resulting from
117 an entrainment-detrainment cycle.

118 Despite the recent discoveries mentioned above, the intra-seasonal dynamics of the ML pump
119 and its potential role in sustaining mesopelagic ecosystems still remains poorly understood. The
120 reason is twofold. First, current methods to estimate the depth of the mixed layer are not
121 appropriate. Brainerd et al. (1995) highlighted the importance in distinguishing the mixed layer,
122 the zone of relatively homogenous water formed by the history of mixing, from the mixing
123 layer, the zone in which mixing is currently active. They showed that current density-derived
124 methods fail to capture the high-frequency variability of the mixing layer. Second, most existing
125 observational tools are not well suited to study such unpredictable episodic and widespread
126 events. Using high-frequency sampling from autonomous profiling floats equipped with bio-
127 optical sensors, we investigate here the intra-seasonal dynamics of the ML pump in the subpolar
128 North Atlantic Ocean, a region that exhibits a strong spatiotemporal variability of the MLD.
129 More specifically, we attempt to quantify the strength of the intra-seasonal ML pump on a basin
130 scale, and characterize the nature and the fate of the exported material in the mesopelagic. The
131 efficiency of this process in terms of long-term sequestration of carbon is not addressed. Rather,
132 we discuss its importance in supplying pulses of fresh organic substrate to the mesopelagic
133 ecosystem.

134

135 **2 Material and Methods**

136 **2.1 The BGC-Argo dataset: description and data processing**

137 The data used in this study were acquired by a fleet of 14 BGC-Argo floats that were deployed
138 in the subpolar North Atlantic Ocean. These floats provided 2126 profiles spanning all seasons
139 between 2014 and 2016 (Fig. 2). These floats (NKE PROVOR CTS-4) were equipped with: an
140 SBE 41 CTD; a WET Labs ECO3 (Combined Three Channel Sensors) composed of a
141 chlorophyll *a* (Chla) fluorometer, a Colored Dissolved Organic Matter (CDOM) fluorometer,
142 and an optical backscattering sensor at 700 nm (b_{bp}); and an OCR-504 radiometer measuring
143 Photosynthetically Available Radiation integrated over 400-700 nm (PAR). Measurements
144 were collected during ascent every 2, 5 or 10 days, from 1,000 m (parking depth) to the surface.
145 Vertical resolution of acquisition was 10 m between 1,000 m and 250 m, 1 m between 250 m
146 and 10 m, and 0.2 m between 10 m and the surface. Radiometric measurements were acquired
147 only in the upper 250 m. Data were transmitted through Iridium communication each time the
148 floats surfaced, usually around local noon.

149 A “real time” quality control procedure was performed on the CTD data (Wong et al., 2015),
150 Chla (Schmechtig et al., 2014) and PAR measurements (Organelli et al., 2016) after the factory
151 calibrations were applied. The instrumental dark signal was removed from the Chla profile
152 following the method in Xing et al. (2011) and the non-photochemical quenching (NPQ) was
153 corrected as follows: the maximum Chla value above MLD, defined as a density difference of
154 0.01 kg m^{-3} with a reference value at 5 m, is extrapolated toward the surface. As an additional
155 condition, the depth of the extrapolated Chla value has to be shallower than the depth of the
156 isolume $20 \mu\text{mol photons m}^{-2} \text{ s}^{-1}$ (derived from smoothed PAR profile), which marks
157 approximately the lower limit of the potential NPQ effect for mixed waters in this area
158 (Lacour et al., 2017; Xing et al., 2018). Chla values were divided by a factor of 2 to account for
159 a calibration systematic error in Wet Labs fluorometers (Roesler et al., 2017). Spikes were
160 removed from Chla and b_{bp} profiles using a 5-point running median filter and a 7-point running
161 mean filter similar to Briggs et al. (2011). The spike signals from b_{bp} profiles were used to
162 detect large particles or aggregates following Briggs et al. (2011). Note that, because of the
163 lower vertical resolution sampling below 250 m, deep spikes are not well resolved which
164 potentially leads to an underestimation of large particles and aggregates. For the same reason,
165 the depth correction for carbon loss relative to b_{bp} in aggregates used by Briggs et al. (2011)
166 was not applied. Both baseline and spike signals from b_{bp} profiles were converted into POC
167 using an empirical factor of $37,537 \text{ mg POC m}^{-2}$ in the mixing layer and $31,519 \text{ mg POC m}^{-2}$
168 below (Cetinić et al., 2012). This relationship might be biased by a background b_{bp} signal that

169 is not necessarily related to POC. Consequently, before converting to POC, the median of deep
 170 (950-1,000 m) b_{bp} values measured by each float was subtracted from each profile of the
 171 corresponding time series. POC derived from the baseline b_{bp} signal likely corresponds to small
 172 particles (0.2-20 μm ; Dall'Olmo & Mork, 2014) whereas POC derived from spike signal
 173 corresponds to large particles or aggregates (Briggs et al., 2011). When not used as POC
 174 proxies, b_{bp} profiles are presented without the correction described above (i.e. removing deep
 175 values).

176

177 **2.2 Atmospheric data**

178 Net heat flux data were extracted from the ECMWF ERA Interim data set (reanalysis), freely
 179 available at <http://apps.ecmwf.int/datasets/data/interim-full-daily/levtype=sfc>. These data were
 180 averaged over 24-hour periods, with spatial resolution of 0.25° .

181 Wind stress data were extracted from the Ifremer CERSAT Global Blended Mean Wind Fields
 182 data set, freely available at <http://marine.copernicus.eu/>. This data set was estimated from
 183 scatterometers ASCAT and OSCAT retrievals and from ECMWF operational wind analysis
 184 with a horizontal resolution of 0.25° and 6 hours in time. Wind stress data were subsequently
 185 averaged over 24-hour periods to match net heat flux data. Wind stress τ was used to calculate
 186 the Ekman vertical length scale as follows: $Z_{Ek} = \gamma \frac{w_*}{f}$, where γ is an empirical constant of
 187 0.5 (Wang & Huang, 2004), $f = 2 \times 7.29 \times 10^{-5} \times \sin(\text{latitude})$ is the Coriolis parameter
 188 and w_* is the turbulent friction velocity $w_* = \sqrt{\frac{\tau}{\rho_w}}$ with ρ_w the density of the surface water.

189

190 **2.3 Estimation of mixing and mixed layer depths**

191 A single criterion, the maximum vertical gradient, was used to estimate the mixing and mixed
 192 layer depths from Chla (maximum negative gradient) and density profiles (maximum positive
 193 gradient), respectively. To suppress the influence of spikes or noise, these profiles were
 194 additionally smoothed (Butterworth filter) before calculating the maximum gradient and the
 195 NPQ correction, which may erase a potential gradient, was performed after calculating the
 196 maximum gradient.

197 The maximum density gradient (MLD_{dens}) is interpreted to match the depth of the seasonal
 198 pycnocline (i.e. mixed layer depth), which is the envelope of the maximum depth reached by
 199 the mixing layer (Brainerd & Gregg, 1995). In contrast, the maximum Chla gradient (MLD_{bio})
 200 should mark the mixing layer depth with time scales typical of phytoplankton growth (Boss &
 201 Behrenfeld, 2010; Zawada et al., 2005) (Fig. 1). The underlying concept is that Chla is

202 homogeneous over the whole mixing layer, if turbulent mixing overcomes vertical variations
203 in the phytoplankton net growth rate (Huisman et al., 1999; Taylor & Ferrari, 2011). Indeed,
204 while phytoplankton cells grow within the euphotic layer, mixing redistributes them throughout
205 the mixing layer. However, as soon as cells are detrained from the mixing layer, the Chla signal
206 starts to decrease in the remnant layer (Murphy & Cowles, 1997), hence intensifying the Chla
207 gradient between mixing and remnant layers (Fig. 1). Figure 3 illustrates how MLD_{bio} can
208 change within 2 days in response to change in atmospheric forcing, while MLD_{dens} remains
209 deep as a signature of the past mixing event (on March 28th). As doubling time of phytoplankton
210 cells is on the order of a day or more (Eppley et al., 1973; Goldman et al., 1979) MLD_{bio} is not
211 likely able to capture the diurnal variability of the mixing layer. Thus, the typical timescale of
212 the MLD_{bio} dynamics is 1-2 days. Considering the difference in timescale between MLD_{bio} and
213 MLD_{dens} , we do not expect to have MLD_{bio} deeper than MLD_{dens} except in summer stratified
214 conditions where phytoplankton can grow a few tens of meters below MLD_{dens} , depending on
215 light penetration (see supplementary Fig. S1). Thus, MLD_{bio} estimation > 100 m deeper than
216 MLD_{dens} is considered as an outlier. These outliers represent only 141 profiles, or 7% of the
217 total data set.

218

219 **2.4 Detection of submesoscale subduction events**

220 Subduction is a 3-dimensional (3D) process involving lateral advection of water masses. Such
221 a lateral advection can be identified on a 1D profile using a state variable called spice, based on
222 anomalous temperature-salinity properties (Flament, 2002; McDougall & Krzysik, 2015;
223 Omand et al., 2015). This variable is a useful indicator of interleaving of water masses. The
224 relative standard deviation of a spice profile (RSD_{spice} , standard deviation / mean) from
225 surface (5 m) to MLD_{dens} is used to detect a potential intrusion of water in this layer. Application
226 of this method over the entire dataset enables to roughly identify the submesoscale subduction
227 events at a basin scale (Llort et al., 2018).

228

229 **3 Results**

230 **3.1 Mixing versus Mixed layer dynamics**

231 As proxies of the mixing and mixed layer depths, MLD_{bio} and MLD_{dens} , show different seasonal
232 dynamics (Fig. 4). MLD_{bio} and MLD_{dens} are similar in fall and early winter, when strong
233 atmospheric forcing induces turbulent mixing down to a depth that will define the upper limit
234 of the seasonal pycnocline. During these periods, temperature, salinity and phytoplankton
235 biomass are homogeneous down to MLD_{dens} . In late winter, MLD_{bio} and MLD_{dens} start to

236 diverge. Shallower mixing layers form above remnant layers, delimited by MLD_{bio} at the top
237 and by MLD_{dens} at the bottom (Fig. 1). Phytoplankton in these remnant layers thus become
238 isolated from the surface layer. In summer, MLD_{bio} is generally deeper than MLD_{dens} and likely
239 corresponds to the lower limit of the euphotic zone. Light penetrates deeper than MLD_{dens} and
240 allows phytoplankton growth below this layer (Fig. S1). Hence, regardless of the season,
241 MLD_{bio} is a good indicator of the depth of the productive layer.

242

243 **3.2 Impact of the mixing layer dynamics on POC export**

244 The time series of a specific float (WMO 6901516, see the float trajectory in Fig. 2) is used to
245 illustrate the impact of the mixing layer dynamics on POC export (Fig. 5). While MLD_{dens}
246 roughly varies at the seasonal time scale, MLD_{bio} varies at higher frequency (Fig. 5b). MLD_{bio}
247 oscillates between MLD_{dens} during convective mixing events (negative net heat flux, see Fig.
248 5c) and a shallower depth during stratification (positive heat flux) or shallow mixing events
249 (i.e. wind-driven mixing, see Z_{EK} on Fig. 5b).

250 High variability of the mixing layer occurs when net heat flux (Q) oscillates around zero during
251 the winter-spring transition (March-May, Fig. 5c). The switch from negative to positive net heat
252 flux is not a rapid smooth transition. Rather, it occurs over more than a one-month period and
253 is associated with an intermittent reversal of the sign of this flux. This intermittency drives the
254 high variability of MLD_{bio} which acts as a physical pump. Interestingly, zero-crossing net heat
255 flux, in fall, does not affect the dynamics of MLD_{bio} which remains closely related to MLD_{dens} .
256 The water mass history of mixing can be retraced using a single 1D profile. Indeed, MLD_{bio}
257 marks the depth limit of recently active mixing, while MLD_{dens} marks the depth limit of past
258 mixing. Thus, the presence of a remnant layer can be identified and used as a signature of the
259 ML pump. However, submesoscale subduction, which involves 3D processes, may also lead to
260 similar signatures (Fig. S2). Therefore, profiles with RSD_{spice} higher than 5% were removed
261 from the analysis in order to focus exclusively on ML pump-driven mechanisms. For the
262 remaining profiles with a ML pump signature, it is assumed that each POC stock isolated in the
263 remnant layer has been exported by the ML pump. In the present study, export is defined as the
264 transfer of carbon from the turbulent productive layer to the low-turbulence remnant layer. In
265 the area sampled by float 6901516, the POC stock transferred by the ML pump is maximal
266 during the winter-spring transition when net heat fluxes switch from negative to positive values
267 (up to 1.1 g C m^{-2} , see Fig. 5d). This maximum occurs before the main spring bloom (Fig. 5d
268 and 5a). Occasionally, the contribution of large particles or aggregates to the POC stock can be
269 significant (up to 88% during the winter-spring transition, see Fig. 5d).

270 On the basin scale, the temporal distribution of POC stocks transferred to the remnant layer
 271 presents a similar pattern. POC stocks significantly increase when the sign of the smoothed heat
 272 flux changes from negative to positive, with maximum values occurring 15 to 30 days later
 273 (Fig. 6a), and appear to be widespread over the whole subpolar region (Fig. 6b). Note that
 274 changing the RSD_{spice} threshold from 2.5 to 10% does not impact the distribution of POC stocks
 275 exported by ML pump events (see Fig. S3).

276

277 **3.3 A quasi-Lagrangian approach to the ML pump**

278 BGC-Argo floats are not Lagrangian floats and thus do not necessarily track coherent water
 279 masses. However, depending on the temporal resolution of the floats, some successive profiles
 280 may sample the same water mass, as evidenced by only subtle changes in hydrographic
 281 properties. Here, within 3 pre-defined layers (surface, remnant and deep layer), we used
 282 temperature, salinity and density differences of 0.1°C, 0.02 psu and 0.01 kg m⁻³ among
 283 consecutive profiles as criteria to identify sections of float trajectories with quasi-Lagrangian
 284 behaviors. We found only two sections that complied with these highly selective criteria (top
 285 panels in Fig. 7a and b). The first section contains 3 profiles from float 6901516 (yellow dots
 286 in Fig. 2) with 2-day intervals, and the second one contains 4 profiles from float 6901480 (green
 287 dots in Fig. 2) also with 2-day intervals. The first profile of each section is well mixed up to
 288 250 m depth and 600 m depth for float 6901516 and 6901480 respectively. Then, mixing stops
 289 and a new mixing layer forms to a depth of around 100 m in both sections. The quasi-
 290 Lagrangian framework allows us to investigate the fate of Chla and b_{bp} within these 3 pre-
 291 defined layers (Fig. 7).

292 In new mixing layers (i.e. surface layers), both Chla and b_{bp} increase as a response to
 293 phytoplankton growth (triangles in Fig. 7). However, the accumulation rate of Chla
 294 ($\frac{1}{Chla} \frac{dChla}{dt} = 0.15 \text{ d}^{-1}$ and 0.16 d^{-1}) is higher than the accumulation rate of b_{bp} ($\frac{1}{b_{bp}} \frac{db_{bp}}{dt} = 0.04 \text{ d}^{-1}$
 295 and 0.05 d^{-1}) for the full section period (4 days and 6 days) of float 6901516 and 6901480
 296 respectively. In remnant layers, located in the twilight zone, both Chla and b_{bp} decrease,
 297 probably as a response to a change in the balance between production and heterotrophic
 298 consumption (circles in Fig. 7). Like surface layers, loss rate (i.e. negative accumulation rate)
 299 of Chla (0.1 d^{-1} and 0.06 d^{-1}) is higher than loss rate of b_{bp} (0.03 d^{-1} and 0.005 d^{-1}) for float
 300 6901516 and 6901480 respectively. In deep layers, Chla and b_{bp} are stable with values near zero
 301 for Chla and values higher than $1 \times 10^{-4} \text{ m}^{-1}$ for b_{bp} (squares in Fig. 7). This deep b_{bp} signal is
 302 considered to be a constant background value.

303 As soon as the remnant layer forms and traps particles at depth, the Chla to b_{bp} ratio in this layer
 304 starts to decrease (Fig. 8). Thus, the Chla to b_{bp} ratio in the remnant layer can be considered as
 305 a relative proxy for the freshness of the exported material. A power law function, similar to the
 306 one used to calculate particle degradation in the ocean interior (Martin et al., 1987), has been
 307 fitted to the data to estimate an attenuation rate. Interestingly, in the remnant layer, the
 308 attenuation rate of the Chla to b_{bp} ratio over time is similar for both floats located in different
 309 regions of the subpolar North Atlantic (similar exponent in equations of Fig. 8a). Time series
 310 of Chla to b_{bp} ratio at each depth along the float trajectories 6901516 (February-July 2014)
 311 show that the ML pump export fresh material to depths ranging 0-340 m (mean 90 m) below
 312 MLD_{bio} during the whole winter-spring transition period (Fig. 9). Hence, the intermittent
 313 behavior of the ML pump in the winter-spring transition generates pulses of fresh organic
 314 material into the mesopelagic zone.

315

316 **3.4 ML pump-driven POC flux estimates**

317 We present here a method to estimate intra-seasonal ML pump-driven POC fluxes. The
 318 approach consists of calculating POC fluxes over a fixed time period on a basin scale (i.e.
 319 spatiotemporal binning), based on independent float profiles, i.e. without any assumption
 320 regarding float Lagrangian behavior.

321 A single ML pump event is defined by three successive steps: shallow mixing at time t_0 (i.e.
 322 initial conditions), deep mixing at time t_1 that leads to the entrainment of deep POC and
 323 restratification that leads to the detrainment of POC and the formation of the remnant layer
 324 observed at time t_2 (Fig. S4). The net POC flux is defined as the difference between the
 325 detrainment and entrainment fluxes, calculated as:

$$\langle E_{entrainment} \rangle = \frac{\langle \int_{z=MLD_{bio,t_0}}^{z=MLD_{dens,t_2}} POC_{t_0}(z) dz \rangle}{2 \langle \Delta t \rangle} \quad (1)$$

$$\langle E_{detrainment} \rangle = \frac{\langle POC_{t_1}(MLD_{dens,t_2} - MLD_{bio,t_2}) \rangle}{2 \langle \Delta t \rangle} \quad (2)$$

$$\langle E_{net} \rangle = \langle E_{detrainment} \rangle - \langle E_{entrainment} \rangle \quad (3)$$

326 The numerator of equation 1 stands for the POC entrained by the deep mixing event at time t_1
 327 while the numerator of equation 2 stands for the POC detrained during the restratification event

328 (Fig. S5). $MLD_{dens\ t_2}$ marks the depth limit of the deep mixing event and ($MLD_{dens\ t_2} -$
 329 $MLD_{bio\ t_2}$) represents the thickness of the remnant layer observed at time t_2 . POC_{t_1} , the POC
 330 concentration within the deep mixing layer at time t_1 , is estimated as the mean POC_{t_0} from the
 331 surface to $MLD_{dens\ t_2}$ (Fig. S5). Brackets indicate spatiotemporal binning. Δt is the time elapsed
 332 between the observation at time t_2 and the last mixing event at time t_1 , and can be derived from
 333 the best-fit power law function in Fig. 8b as:

$$\Delta t = t_2 - t_1 = \left(\frac{Chla/b_{bp\ t_2} - Chla/b_{bp\ t_1}}{-0.11\ Chla/b_{bp\ t_1}} \right)^{\frac{1}{0.55}} \quad (4)$$

334 where $Chla/b_{bp\ t_2}$ is the ratio of the median Chla to the median b_{bp} within the remnant layer
 335 and $Chla/b_{bp\ t_1}$ is the ratio within the deep mixing layer at time t_1 . $Chla/b_{bp\ t_1}$ is estimated
 336 the same way as POC_{t_1} , by averaging $Chla_{t_0}$ and $b_{bp\ t_0}$ from the surface to $MLD_{dens\ t_2}$. While
 337 $Chla/b_{bp\ t_2}$, $MLD_{dens\ t_2}$, and $MLD_{bio\ t_2}$ are measured at time t_2 when a remnant layer is
 338 identified (i.e. ML pump signature), initial conditions prevailing at time t_0 (i.e.
 339 $MLD_{bio\ t_0}$, POC_{t_0} , $Chla_{t_0}$, $b_{bp\ t_0}$), from which variable at time t_1 are derived, are unknown. In
 340 order to provide a set of potential initial conditions for each profile with a ML pump signature,
 341 all available profiles, from 2014 to 2016, within a radius of 300 km and a time period of 15
 342 days (all years included), are collected (Fig. S6). To keep only realistic initial conditions, three
 343 requisites are needed: 1) $Chla/b_{bp\ t_1}$, derived from $Chla_{t_0}$ and $b_{bp\ t_0}$, is higher than
 344 $Chla/b_{bp\ t}$, 2) $MLD_{bio\ t_0}$ is shallower than $MLD_{dens\ t_2}$, 3) Δt is less than 20 days. The choice
 345 of a threshold of 20 days is based on the basin-scale analysis of the density function of
 346 $Chla/b_{bp}$ both within the mixing and remnant layers (Fig. S7). Using the attenuation rate of
 347 $Chla/b_{bp}$ shown in Fig. 8b, we modeled the cumulative density function within the remnant
 348 layer for Δt ranging from 1 to 5, 20 or 35 days (see caption of Fig. S7) and compared it with
 349 the measured cumulative density function. The cumulative density function for Δt ranging from
 350 1 to 20 days is the one which best fit the measured density function within the remnant layer.
 351 Therefore, a threshold of 20 days seems appropriate to reject unrealistic initial conditions. All
 352 the initial conditions that complied with these 3 requisites are used to calculate a mean Δt and
 353 associated standard deviation for each profile presenting a ML pump signature. Over a fixed
 354 time period, the mean duration of ML pump events is estimated as $2 < \Delta t >$ (Fig. S8). Indeed,
 355 as the profiling time t_2 is random between the last mixing event at time t_1 and the next one,

356 potentially at t_3 , Δt should range from 0 to $(t_3 - t_1)$, with mean value $\langle \Delta t \rangle = (t_3 - t_1)/2$.
357 Here, a time period of 10 days is used, with a minimum of 6 profiles as an additional
358 requirement to correctly estimate the mean duration of ML pump events.
359 Figure 10 presents estimates of entrainment, detrainment and net POC fluxes averaged over 10-
360 day periods in the whole subpolar North Atlantic Ocean. As expected, the temporal pattern in
361 detrainment fluxes (Fig. 10c) is similar to the one observed in POC stock in the remnant layer
362 (Fig. 6a) and the one in detrained POC stocks estimated from initial conditions (Fig. 10a,
363 numerators in equation 2, blue color). Maximum detrainment fluxes and net export fluxes (125
364 and $55 \text{ mg C m}^{-2} \text{ d}^{-1}$, respectively) both occur few days after the switch in the sign of the heat
365 flux. Approximately 40 days later, detrainment fluxes decrease by a factor of 2 to 3 and net
366 POC fluxes are reduced to near zero. The length of error bars represents the average standard
367 deviation of initial conditions associated to each ML pump signature detected within a 10-day
368 time period. Note that fluxes were not estimated between days 70 to 90 because the number of
369 profiles presenting a ML pump signature was below the critical threshold of 6 profiles (Fig.
370 S8).

371

372 **4 Discussion**

373 **4.1 Mixing versus mixed layer depth**

374 Observations of vertical profiles of density and Chla in late winter and spring (Fig. 4) suggest
375 that density-derived methods to estimate MLD have to be interpreted with caution when
376 considering controls on phytoplankton processes. A simple comparison (linear correlation
377 analysis, Fig. S9) between MLD_{bio} and MLD estimated with different density-difference criteria
378 revealed that most of these criteria do not detect subtle changes in density, which affect the
379 phytoplankton vertical distribution (Lacour et al., 2017). As a consequence, studies estimating
380 depth-integrated Chla by multiplying the concentration of surface Chla (measured by satellite)
381 by the depth of a density-derived mixed layer could overestimate the Chla stock, especially
382 during the winter to spring transition. Indeed, the widely used density difference criteria of 0.1
383 kg m^{-3} leads, in the present study, to a mean overestimation of 46% of the spring phytoplankton
384 stock (comparison of the real stock measured by the float in the mixed layer with the estimated
385 stock based on surface Chla). However, a density criterion of 0.01 kg m^{-3} , which shows the best
386 correlation with MLD_{bio} , leads to a mean overestimation of only 3%. Most density difference
387 thresholds are not suited to capture the intra-seasonal dynamics of the mixing layer which
388 affects the vertical distribution of phytoplankton biomass.

389

390 **4.2 The ML pump signature**

391 The ML pump is a complex mechanism which can occur on a variety of timescales, from diurnal
392 to seasonal scales. Observing this mechanism at specific scales requires appropriate approaches.
393 Combining Argo float data with satellite estimates of POC, Dall'Olmo et al. (2016) provided
394 first estimates of the carbon flux induced by the seasonal ML pump at global scale. The rate of
395 change of the MLD at a time interval of 10 days along Argo float trajectories was exploited.
396 Therefore, the high-frequency variability (< 10 days) was not considered and assumption of
397 spatial homogeneity was required. This approach revealed the importance of the ML pump in
398 seasonal carbon fluxes but the episodic nature of carbon export was not considered. The
399 innovative approach, here, is to use a single profile to retrace the water mass history of mixing
400 and thus relax the assumption of spatial homogeneity. Using MLD_{bio} as the depth limit of a
401 recent mixing and MLD_{dens} as the depth limit of a past mixing, the presence of a remnant layer
402 can be identified and used as a signature of the ML pump. Although the typical timescale of
403 MLD_{bio} is known (~1-2 days), the timescale of MLD_{dens} is more difficult to assess. Figure 3b
404 shows that MLD_{dens} is still deep 4 days after deep convection stopped and figure 5b reveals a
405 ~10-day delay between the permanent shoaling of MLD_{bio} around 100 m and the shoaling of
406 MLD_{dens} . It is thus assumed that MLD_{dens} roughly corresponds to a mixed layer on a 10-day
407 timescale. Thereby, the signature of ML pump likely reveals recent export of organic matter
408 thus allowing the assessment of the episodic nature of this mechanism. Although this approach
409 allows exploration of the intra-seasonal dynamics of the ML pump, the diurnal timescales are
410 not assessed.

411 The strongest signatures of the ML pump (i.e. maximum POC stock in the remnant layer) were
412 recorded when the net heat flux switches from negative to positive values in early spring.
413 Interestingly, the switch from positive to negative values in fall did not affect MLD_{bio} which
414 remained closely related to MLD_{dens} (Fig. 5). This dissymmetry was likely due to the
415 mechanical effect of wind, that mixes the upper layer (Woods, 1980). The Ekman length scale,
416 which is the dominant mixing length scale when heat fluxes are small (Brody & Lozier, 2014),
417 indicated that mixing reached depths as deep as MLD_{dens} at this time of the year (Fig. 5b).
418 Phytoplankton can be redistributed within MLD_{dens} even if net heat fluxes become positive,
419 thus inhibiting the formation of remnant layers.

420 Warming of the upper layer is not the only source of stratification. In addition to freshwater
421 flux, 3D processes involving lateral advection are known to quickly restratify deep mixed layers
422 (Brainerd & Gregg, 1993; Hosegood et al., 2006, 2008; Johnson et al., 2016). Submesoscale
423 eddies or Ekman buoyancy flux can slump horizontal density gradient to create vertical

424 stratification (Boccaletti et al., 2007; Thomas & Lee, 2005). These processes, which generate a
425 signature similar to the ML pump, are often associated with submesoscale subduction (Omand
426 et al., 2015). Based on a RSD_{spice} threshold of 5%, it can be estimated that almost 40% of the
427 profiles displaying a ML pump signature were affected by lateral water intrusion. As mentioned
428 by Ho and Marra (1994), quantifying ML pump export is difficult since local and advective
429 effects have to be distinguished. Here, a RSD_{spice} threshold of 5% appeared adequate to identify
430 and subsequently remove profiles affected by advective effects. However, it is worth noting
431 that lateral restratifications could contribute to the export through the ML pump. Indeed, lateral
432 restratification can stimulate phytoplankton production (Mahadevan et al., 2012), even during
433 winter (Lacour et al., 2017), and the resulting biomass could be exported later, following a deep
434 mixing event. Although this study focuses on 1D processes, lateral restratification may also
435 stimulate the ML pump export, especially in winter when positive heat flux events are scarcer.
436

437 **4.3 Fate of Chla and b_{bp} signal in the remnant layer**

438 Quasi-Lagrangian sections of float trajectories allowed us to investigate the fate of Chla and b_{bp}
439 signals in surface and remnant layers after a stratification event (Fig. 7). Chla signals increased
440 faster in the surface layer and decreased faster in the remnant layer than the b_{bp} signals. The
441 main reason for this discrepancy rests on the nature of the particles contributing to both Chla
442 and b_{bp} signal. While phytoplankton cells contribute nearly all of the Chla signal (colored
443 dissolve organic matter may also contribute slightly to the Chla signal; Xing et al., 2017),
444 bacteria, protists, detritus and mineral material also contribute to the b_{bp} signal (Martinez-
445 Vicente et al., 2012; Stramski et al., 1991, 2001, 2004). Therefore, in the surface layer, an
446 increase in phytoplankton production does not lead to a similar relative increase in the Chla and
447 b_{bp} signals. In addition, taxonomic changes in the phytoplankton community could further
448 increase the Chla signal relative to the b_{bp} signal. Indeed, the local restratification could enhance
449 the light environment and stimulate larger phytoplankton, such as diatoms, with higher Chla to
450 b_{bp} ratio (Cetinić et al., 2015; Lacour et al., 2017; Rembauville et al., 2017). In the twilight
451 remnant layer, change in the balance between production and consumption leads to a decrease
452 in both Chla and b_{bp} . However, the faster decrease in the Chla signal may be explained by
453 multiple factors. First, fresh phytoplankton (i.e. Chla signal) are possibly preferentially
454 consumed compared to detritus and other material contributing to the b_{bp} signal. Second, the
455 consumption of phytoplankton cells could enhance the growth of heterotrophic organisms such
456 as bacteria or protists which would also contribute to the b_{bp} signal. Third, physical and
457 biological disaggregation of large particles at depth (Alldredge et al., 1990; Burd & Jackson,

458 2009; Cho & Azam, 1988) may enhance the b_{bp} signal, which likely corresponds to small
459 particles (0.2-20 μm ; Dall’Olmo & Mork, 2014), and counteract the decrease in b_{bp} due to
460 consumption. Finally, additional decrease in Chla could be attributed to physiological
461 adaptations to darkness which involve a reduced fluorescence per unit of Chla (Murphy &
462 Cowles, 1997).

463

464 **4.4 Towards global event-based POC flux estimates**

465 Present carbon flux estimates are mainly based on a limited number of observations at specific
466 times and locations. Scaling up these observations to obtain regional and global estimates may
467 neglect or underestimate the contribution of episodic events, leading to our inability to balance
468 biogeochemical budgets in the mesopelagic (Burd et al., 2016). The ML pump is a typical
469 mechanism driving episodic export of organic carbon to depth. Based on high-resolution
470 observations from a dense BGC-Argo float network, we assessed for the first time the intra-
471 seasonal dynamics of ML pump-driven POC fluxes on a basin scale (Fig. 10). This approach
472 required three main assumptions:

473 (1) We assumed that initial conditions (i.e. Chla/b_{bp} $_{t_0}$, $\text{POC}_{\text{MLD}_{\text{bio}}}$ $_{t_0}$) prevailing before a

474 ML pump event can be predicted from a “climatology” of profiles collected in the area
475 of the event location. Three selection criteria (see section 3.4) have been applied to
476 ensure that only realistic initial conditions have been used. Error bars in figure 10a and
477 b show that the variability related to these initial conditions remains reasonably small.

478 (2) We assumed that the mean duration of ML pump events is twice the mean time $\langle \Delta t \rangle$
479 between the observation of the ML pump signature and the last mixing event. An
480 analysis of ML pump events recorded by a Lagrangian float revealed that the absolute
481 error related to this assumption is less than 0.2 days as long as the number of events
482 averaged is more than 6 (Fig. S6). As the BGC-Argo dataset will expand in the future,
483 we will be able to reduce the spatiotemporal binning with the goal of quantifying event-
484 based POC fluxes on a basin scale.

485 (3) The attenuation rate of the Chla to b_{bp} ratio in the remnant layer is assumed to be
486 constant on a basin scale. The present analysis demonstrated that this attenuation rate is
487 similar within two different regions of the subpolar North Atlantic. However, additional
488 measurements in remnant layers are clearly needed to better constrain the attenuation
489 rate of the Chla to b_{bp} ratio and reduce uncertainties associated to this approach. More
490 generally, further investigations on particle composition, microbial metabolism and

491 transformation processes occurring in remnant layers are required to better understand
492 the fate of the organic material exported by the ML pump.

493 The mean ML pump-driven net POC flux peaks at $55 \text{ mg C m}^{-2} \text{ d}^{-1}$ in late winter and drops
494 down to negative values when the water column stabilizes in summer. During this period, the
495 entrainment flux due to wind-driven mixing events can exceed the detrainment flux, as the light
496 penetration allows phytoplankton to grow below the mixing layer. The net amount of POC
497 exported during the winter-spring transition (i.e. positive net export) is the fraction of fresh
498 organic material that we expect to be consumed in the mesopelagic. Therefore, the intra-
499 seasonal ML pump may sustain the mesopelagic ecosystem before the spring bloom period.

500

501 **4.5 Role of the ML pump in sustaining mesopelagic ecosystems**

502 The recurrence of widespread ML pump events during a relatively large time period (> 90 days)
503 implies that this mechanism may be of great significance in supplying the energy required by
504 the mesopelagic heterotrophic community (Dall'Olmo et al., 2016). The particles mixed
505 downward through the ML pump are rich in fresh phytoplankton and detritus, so potentially of
506 high nutritional content for grazers located below the mixing layer (Steinberg & Landry, 2017).
507 Export of both small and large particles to the mesopelagic region suggests that this mechanism
508 could sustain zooplankton populations with different feeding preferences (Fenchel, 1980;
509 Irigoien et al., 2000; Turner et al., 2001; Turner, 2004). Products from zooplankton activities
510 would then sustained microbial populations and higher trophic levels (Steinberg & Landry,
511 2017). Therefore, the ML pump could supply a major source of energy to the whole
512 mesopelagic ecosystem during the winter to spring transition.

513 Many studies reported that the bulk of zooplankton populations resides just below the turbulent
514 mixing layer (Incze et al., 2001; Lagadeuc et al., 1997; Mackas et al., 1993). The turbulence-
515 avoidance behavior of grazers has been invoked to explain their vertical distribution in the water
516 column (Franks, 2001). However, the reason for this behavior is not clear. Turbulence is known
517 to influence encounter and ingestion rate of zooplankton and larger predators, but both positive
518 and negative effects have been reported (MacKenzie, 2000). During the winter to spring
519 transition, the vertical distribution of grazers could be a direct consequence of the ML pump.
520 These organisms could swim deep during turbulent mixing events, then immediately return to
521 the remnant layer upon restratification to take advantage of fresh food supplied by the ML
522 pump. For this reason, export is defined here as a transfer from the turbulent productive layer
523 to the remnant non-productive layer.

524 Finally, the ML pump during the winter-spring transition could trigger the seasonal
525 development of overwintering organisms such as copepods so that their reproduction would
526 coincide with the forthcoming spring bloom (Bishop & Wood, 2009). We can thus speculate
527 that the frequency of episodic ML pump export events during the pre-bloom period may
528 modulate the timing of the maturation phase of copepods and indirectly impact the magnitude
529 of the spring bloom.

530

531 **5 Conclusion**

532 The density of the BGC-Argo float network has enabled, for the first time, investigation of the
533 intra-seasonal dynamics of the ML pump on a basin scale. ML pump signatures are widespread
534 over the subpolar North Atlantic Ocean and span a large temporal window preceding the spring
535 bloom. To date, the high-frequency dynamics of bio-physical mechanisms had clearly been
536 overlooked due to the lack of well-suited observational tools. Yet, ML pump episodic events
537 may contribute significantly to the export of fresh organic matter during the late winter and
538 early spring periods. This mechanism may sustain the development of overwintering organisms
539 such as copepods with potential impact on the characteristics of the forthcoming spring
540 phytoplankton bloom through predator-prey interactions. Further investigations of episodic
541 events will undoubtedly provide new insights on life strategies and food web interactions, and
542 potentially address the fundamental limitations of assuming steady-state conditions.

543

544 **Acknowledgments**

545 This work represents a contribution to the REMOCEAN project (REMOtely sensed
546 biogeochemical cycles in the OCEAN, GA 246777) funded by the European Research Council
547 and the ATLANTOS EU project (grant agreement 2014-633211) funded by H2020 program.
548 BGC-Argo data are publicly available at <ftp://ftp.ifremer.fr/ifremer/argo/dac/coriolis/>. We
549 thank C. Schmechtig and A. Poteau for BGC-Argo float data management and M. Gali for
550 fruitful discussions.

551

552 **References**

- 553 Alldredge, A. L., Granata, T. C., Gotschalk, C. C., & Dickey, T. D. (1990). The physical
554 strength of marine snow and its implications for particle disaggregation in the ocean.
555 *Limnology and Oceanography*, 35(7), 1415–1428.
556 <https://doi.org/10.4319/lo.1990.35.7.1415>
- 557 Barth, J. A., Cowles, T. J., Kosro, P. M., Shearman, R. K., Huyer, A., & Smith, R. L. (2002).
558 Injection of carbon from the shelf to offshore beneath the euphotic zone in the California
559 Current. *Journal of Geophysical Research*, 107(C6), 3057.

- 560 <https://doi.org/10.1029/2001JC000956>
- 561 Bishop, J. K. B., Conte, M. H., Wiebe, P. H., Roman, M. R., & Langdon, C. (1986).
 562 Particulate matter production and consumption in deep mixed layers: observations in a
 563 warm-core ring. *Deep Sea Research Part A. Oceanographic Research Papers*, 33(11–
 564 12), 1813–1841. [https://doi.org/10.1016/0198-0149\(86\)90081-6](https://doi.org/10.1016/0198-0149(86)90081-6)
- 565 Bishop, J. K. B., & Wood, T. J. (2009). Year-round observations of carbon biomass and flux
 566 variability in the Southern Ocean. *Global Biogeochemical Cycles*, 23(2), n/a-n/a.
 567 <https://doi.org/10.1029/2008GB003206>
- 568 Boccaletti, G., Ferrari, R., & Fox-Kemper, B. (2007). Mixed Layer Instabilities and
 569 Restratification. *Journal of Physical Oceanography*, 37(9), 2228–2250.
 570 <https://doi.org/10.1175/JPO3101.1>
- 571 Boss, E., & Behrenfeld, M. (2010). In situ evaluation of the initiation of the North Atlantic
 572 phytoplankton bloom. *Geophysical Research Letters*, 37(18).
 573 <https://doi.org/10.1029/2010GL044174>
- 574 Brainerd, K. E., & Gregg, M. C. (1993). Diurnal restratification and turbulence in the oceanic
 575 surface mixed layer: 1. Observations. *Journal of Geophysical Research*, 98(C12), 22645.
 576 <https://doi.org/10.1029/93JC02297>
- 577 Brainerd, K. E., & Gregg, M. C. (1995). Surface mixed and mixing layer depths. *Deep-Sea*
 578 *Research Part I*, 42(9), 1521–1543. [https://doi.org/10.1016/0967-0637\(95\)00068-H](https://doi.org/10.1016/0967-0637(95)00068-H)
- 579 Briggs, N., Perry, M. J., Cetinić, I., Lee, C., D’Asaro, E., Gray, A. M., & Rehm, E. (2011).
 580 High-resolution observations of aggregate flux during a sub-polar North Atlantic spring
 581 bloom. *Deep Sea Research Part I: Oceanographic Research Papers*, 58(10), 1031–1039.
 582 <https://doi.org/10.1016/j.dsr.2011.07.007>
- 583 Brody, S. R., & Lozier, M. S. (2014). Changes in dominant mixing length scales as a driver of
 584 subpolar phytoplankton bloom initiation in the North Atlantic. *Geophysical Research*
 585 *Letters*, 41(9), 3197–3203. <https://doi.org/10.1002/2014GL059707>
- 586 Buesseler, K. O., & Boyd, P. W. (2009). Shedding light on processes that control particle
 587 export and flux attenuation in the twilight zone of the open ocean. *Limnology and*
 588 *Oceanography*, 54(4), 1210–1232. <https://doi.org/10.4319/lo.2009.54.4.1210>
- 589 Burd, A. B., Hansell, D. A., Steinberg, D. K., Anderson, T. R., Arístegui, J., Baltar, F., ...
 590 Tanaka, T. (2010). Assessing the apparent imbalance between geochemical and
 591 biochemical indicators of meso- and bathypelagic biological activity: What the @#! is
 592 wrong with present calculations of carbon budgets? *Deep-Sea Research Part II: Topical*
 593 *Studies in Oceanography*, 57(16), 1557–1571. <https://doi.org/10.1016/j.dsr2.2010.02.022>
- 594 Burd, A. B., & Jackson, G. A. (2009). Particle Aggregation. *Annual Review of Marine*
 595 *Science*, 1(1), 65–90. <https://doi.org/10.1146/annurev.marine.010908.163904>
- 596 Burd, A., Buchan, A., Church, M., Landry, M., McDonnell, A., Passow, U., ... Benway, H.
 597 (2016). *Towards a transformative understanding of the ocean ’ s biological pump :*
 598 *Priorities for future research. Report of the NSF Biology of the Biological Pump*
 599 *Workshop, February 19-20, 2016*. Woods Hole, MA: Ocean Carbon and
 600 Biogeochemistry (OCB) Program. <https://doi.org/10.1575/1912/8263>
- 601 Carlson, C. A., Ducklow, H. W., & Michaels, A. F. (1994). Annual flux of dissolved organic
 602 carbon from the euphotic zone in the northwestern Sargasso Sea. *Nature*, 371(6496),
 603 405–408. <https://doi.org/10.1038/371405a0>
- 604 Cetinić, I., Perry, M. J., Briggs, N. T., Kallin, E., D’Asaro, E. a., & Lee, C. M. (2012).
 605 Particulate organic carbon and inherent optical properties during 2008 North Atlantic
 606 Bloom Experiment. *Journal of Geophysical Research*, 117(C6), C06028.
 607 <https://doi.org/10.1029/2011JC007771>
- 608 Cetinić, I., Perry, M. J., D’Asaro, E., Briggs, N., Poulton, N., Sieracki, M. E., & Lee, C. M.
 609 (2015). A simple optical index shows spatial and temporal heterogeneity in

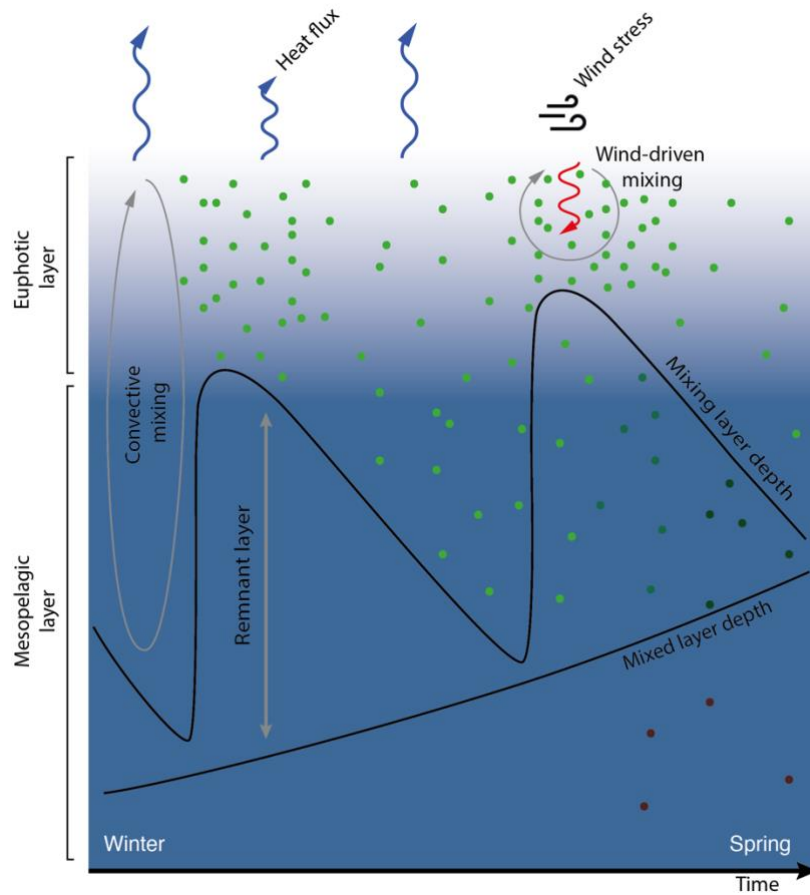
- 610 phytoplankton community composition during the 2008 North Atlantic Bloom
611 Experiment. *Biogeosciences*, 12(7), 2179–2194. [https://doi.org/10.5194/bg-12-2179-](https://doi.org/10.5194/bg-12-2179-2015)
612 2015
- 613 Cho, B. C., & Azam, F. (1988). Major role of bacteria in biogeochemical fluxes in the ocean's
614 interior. *Nature*. <https://doi.org/10.1038/332441a0>
- 615 Dall'Olmo, G., Dingle, J., Polimene, L., Brewin, R. J. W., & Claustre, H. (2016). Substantial
616 energy input to the mesopelagic ecosystem from the seasonal mixed-layer pump. *Nature*
617 *Geoscience*. <https://doi.org/10.1038/ngeo2818>
- 618 Dall'Olmo, G., & Mork, K. A. (2014). Carbon export by small particles in the Norwegian
619 Sea. *Geophysical Research Letters*, 41(8), 2921–2927.
620 <https://doi.org/10.1002/2014GL059244>
- 621 Ducklow, H., Steinberg, D., & Buesseler, K. (2001). Upper Ocean Carbon Export and the
622 Biological Pump. *Oceanography*, 14(4), 50–58. <https://doi.org/10.5670/oceanog.2001.06>
- 623 Eppley, R. W., Renger, E. H., Venrick, E. L., Mullin, M. M., & Jul, N. (1973). A Study of
624 Plankton Dynamics and Nutrient Cycling in the Central Gyre of the North Pacific Ocean.
625 *Limnology and Oceanography*, 18(4), 534–551.
626 <https://doi.org/10.4319/lo.1973.18.4.0534>
- 627 Fenchel, T. (1980). Suspension feeding in ciliated protozoa: Functional response and particle
628 size selection. *Microbial Ecology*, 6(1), 1–11. <https://doi.org/10.1007/BF02020370>
- 629 Franks, P. J. S. (2001). Turbulence avoidance: An alternate explanation of turbulence-
630 enhanced ingestion rates in the field. *Limnology and Oceanography*, 46(4), 959–963.
631 <https://doi.org/10.4319/lo.2001.46.4.0959>
- 632 Gardner, W. D., Chung, S. P., Richardson, M. J., & Walsh, I. D. (1995). The oceanic mixed-
633 layer pump. *Deep Sea Research Part II: Topical Studies in Oceanography*, 42(2–3),
634 757–775. [https://doi.org/10.1016/0967-0645\(95\)00037-Q](https://doi.org/10.1016/0967-0645(95)00037-Q)
- 635 Garside, C., & Garside, J. C. (1993). The “f-ratio” on 20°W during the North Atlantic Bloom
636 Experiment. *Deep-Sea Research Part II*, 40(1–2), 75–90. [https://doi.org/10.1016/0967-](https://doi.org/10.1016/0967-0645(93)90007-A)
637 0645(93)90007-A
- 638 Giering, S. L. C., Sanders, R., Lampitt, R. S., Anderson, T. R., Tamburini, C., Boutrif, M., ...
639 Mayor, D. J. (2014). Reconciliation of the carbon budget in the ocean's twilight zone.
640 *Nature*, 507(7493), 480–483. <https://doi.org/10.1038/nature13123>
- 641 Giering, S. L. C., Sanders, R., Martin, A. P., Lindemann, C., Möller, K. O., Daniels, C. J., ...
642 St. John, M. A. (2016). High export via small particles before the onset of the North
643 Atlantic spring bloom. *Journal of Geophysical Research: Oceans*, 121(9), 6929–6945.
644 <https://doi.org/10.1002/2016JC012048>
- 645 Goldman, J. C., McCarthy, J. J., & Peavey, D. G. (1979). Growth rate influence on the
646 chemical composition of phytoplankton in oceanic waters. *Nature*, 279(5710), 210–215.
647 <https://doi.org/10.1038/279210a0>
- 648 Ho, C., & Marra, J. (1994). Early-spring export of phytoplankton production in the northeast
649 Atlantic Ocean. *Marine Ecology Progress Series*, 114(1), 197–202.
650 <https://doi.org/10.3354/meps114197>
- 651 Hosegood, P., Gregg, M. C., & Alford, M. H. (2006). Sub-mesoscale lateral density structure
652 in the oceanic surface mixed layer. *Geophysical Research Letters*, 33(22), L22604.
653 <https://doi.org/10.1029/2006GL026797>
- 654 Hosegood, P. J., Gregg, M. C., & Alford, M. H. (2008). Restratification of the Surface Mixed
655 Layer with Submesoscale Lateral Density Gradients: Diagnosing the Importance of the
656 Horizontal Dimension. *Journal of Physical Oceanography*, 38(11), 2438–2460.
657 <https://doi.org/10.1175/2008JPO3843.1>
- 658 Huisman, J., Oostveen, P. van, & Weissing, F. J. (1999). Critical Depth and Critical
659 Turbulence: Two Different Mechanisms for the Development of Phytoplankton Blooms.

- 660 *Limnology and Oceanography*, 44(7), 1781–1787. Retrieved from
 661 <http://www.jstor.org/stable/2670414>
- 662 Incze, L., Hebert, D., Wolff, N., Oakey, N., & Dye, D. (2001). Changes in copepod
 663 distributions associated with increased turbulence from wind stress. *Marine Ecology*
 664 *Progress Series*, 213, 229–240. <https://doi.org/10.3354/meps213229>
- 665 Irigoien, X., Harris, R. P., Head, R. N., & Harbour, D. (2000). The influence of diatom
 666 abundance on the egg production rate of *Calanus helgolandicus* in the English Channel.
 667 *Limnology and Oceanography*, 45(6), 1433–1439.
 668 <https://doi.org/10.4319/lo.2000.45.6.1433>
- 669 Johnson, L., Lee, C. M., & D'Asaro, E. A. (2016). Global Estimates of Lateral Springtime
 670 Restratification. *Journal of Physical Oceanography*, 46(5), 1555–1573.
 671 <https://doi.org/10.1175/JPO-D-15-0163.1>
- 672 Jónasdóttir, S. H., Visser, A. W., Richardson, K., & Heath, M. R. (2015). Seasonal copepod
 673 lipid pump promotes carbon sequestration in the deep North Atlantic. *Proceedings of the*
 674 *National Academy of Sciences*, 112(39), 12122–12126.
 675 <https://doi.org/10.1073/pnas.1512110112>
- 676 Koeve, W., Pollehne, F., Oschlies, A., & Zeitzschel, B. (2002). Storm-induced convective
 677 export of organic matter during spring in the northeast Atlantic Ocean. *Deep-Sea*
 678 *Research Part I: Oceanographic Research Papers*, 49(8), 1431–1444.
 679 [https://doi.org/10.1016/S0967-0637\(02\)00022-5](https://doi.org/10.1016/S0967-0637(02)00022-5)
- 680 Kwon, E. Y., Primeau, F., & Sarmiento, J. L. (2009). The impact of remineralization depth on
 681 the air-sea carbon balance. *Nature Geoscience*, 2(9), 630–635.
 682 <https://doi.org/10.1038/ngeo612>
- 683 Lacour, L., Ardyna, M., Stec, K. F., Claustre, H., Prieur, L., Poteau, A., ... Iudicone, D.
 684 (2017). Unexpected winter phytoplankton blooms in the North Atlantic subpolar gyre.
 685 *Nature Geoscience*, 10(11), 836–839. <https://doi.org/10.1038/NGEO3035>
- 686 Lagadeuc, Y., Boulé, M., & Dodson, J. J. (1997). Effect of vertical mixing on the vertical
 687 distribution of copepods in coastal waters. *Journal of Plankton Research*, 19(9), 1183–
 688 1204. <https://doi.org/10.1093/plankt/19.9.1183>
- 689 Lampitt, R. S., Salter, I., de Cuevas, B. A., Hartman, S., Larkin, K. E., & Pebody, C. A.
 690 (2010). Long-term variability of downward particle flux in the deep northeast Atlantic:
 691 Causes and trends. *Deep-Sea Research Part II: Topical Studies in Oceanography*,
 692 57(15), 1346–1361. <https://doi.org/10.1016/j.dsr2.2010.01.011>
- 693 Lévy, M., Klein, P., & Treguier, A.-M. (2001). Impact of sub-mesoscale physics on
 694 production and subduction of phytoplankton in an oligotrophic regime. *Journal of*
 695 *Marine Research*, 59(4), 535–565. <https://doi.org/10.1357/002224001762842181>
- 696 Llort, J., Langlais, C., Matear, R., Moreau, S., Lenton, A., & Strutton, P. G. (2018).
 697 Evaluating Southern Ocean Carbon Eddy-Pump From Biogeochemical-Argo Floats.
 698 *Journal of Geophysical Research: Oceans*, 123(2), 971–984.
 699 <https://doi.org/10.1002/2017JC012861>
- 700 Mackas, D. L., Sefton, H., Miller, C. B., & Raich, A. (1993). Vertical habitat partitioning by
 701 large calanoid copepods in the oceanic subarctic Pacific during Spring. *Progress in*
 702 *Oceanography*, 32(1), 259–294. [https://doi.org/10.1016/0079-6611\(93\)90017-8](https://doi.org/10.1016/0079-6611(93)90017-8)
- 703 MacKenzie, B. R. (2000). Turbulence, larval fish ecology and fisheries recruitment: a review
 704 of field studies. *Oceanologica Acta*, 23(4), 357–375. [https://doi.org/10.1016/S0399-1784\(00\)00142-0](https://doi.org/10.1016/S0399-1784(00)00142-0)
- 705
- 706 Mahadevan, a., D'Asaro, E., Lee, C., & Perry, M. J. (2012). Eddy-Driven Stratification
 707 Initiates North Atlantic Spring Phytoplankton Blooms. *Science*, 337(6090), 54–58.
 708 <https://doi.org/10.1126/science.1218740>
- 709 Martin, J. H., Knauer, G. A., Karl, D. M., & Broenkow, W. W. (1987). VERTEX: carbon

- 710 cycling in the northeast Pacific. *Deep Sea Research Part A. Oceanographic Research*
 711 *Papers*, 34(2), 267–285. [https://doi.org/https://doi.org/10.1016/0198-0149\(87\)90086-0](https://doi.org/https://doi.org/10.1016/0198-0149(87)90086-0)
- 712 Martin, P., Lampitt, R. S., Jane Perry, M., Sanders, R., Lee, C., & D'Asaro, E. (2011). Export
 713 and mesopelagic particle flux during a North Atlantic spring diatom bloom. *Deep Sea*
 714 *Research Part I: Oceanographic Research Papers*, 58(4), 338–349.
 715 <https://doi.org/10.1016/j.dsr.2011.01.006>
- 716 Martinez-Vicente, V., Tilstone, G., Sathyendranath, S., Miller, P., & Groom, S. (2012).
 717 Contributions of phytoplankton and bacteria to the optical backscattering coefficient over
 718 the Mid-Atlantic Ridge. *Marine Ecology Progress Series*, 445, 37–51.
 719 <https://doi.org/10.3354/meps09388>
- 720 Murphy, A. M., & Cowles, T. J. (1997). Effects of darkness on multi-excitation in vivo
 721 fluorescence and survival in a marine diatom. *Limnology and Oceanography*, 42(6),
 722 1444–1453. <https://doi.org/10.4319/lo.1997.42.6.1444>
- 723 Omand, M. M., D'Asaro, E. A., Lee, C. M., Perry, M. J., Briggs, N., Cetinić, I., &
 724 Mahadevan, A. (2015). Eddy-driven subduction exports particulate organic carbon from
 725 the spring bloom. *Science*, 348(6231), 222–225. <https://doi.org/10.1126/science.1260062>
- 726 Organelli, E., Claustre, H., Bricaud, A., Schmechtig, C., Poteau, A., Xing, X., ... Vellucci, V.
 727 (2016). A novel near-real-time quality-control procedure for radiometric profiles
 728 measured by bio-argo floats: Protocols and performances. *Journal of Atmospheric and*
 729 *Oceanic Technology*, 33(5), 937–951. <https://doi.org/10.1175/JTECH-D-15-0193.1>
- 730 Poulton, A. J., Holligan, P. M., Hickman, A., Kim, Y.-N., Adey, T. R., Stinchcombe, M. C.,
 731 ... Woodward, E. M. S. (2006). Phytoplankton carbon fixation, chlorophyll-biomass and
 732 diagnostic pigments in the Atlantic Ocean. *Deep Sea Research Part II: Topical Studies*
 733 *in Oceanography*, 53(14–16), 1593–1610. <https://doi.org/10.1016/j.dsr2.2006.05.007>
- 734 Price, J. F., Weller, R. A., & Pinkel, R. (1986). Diurnal Cyciling: Observation and models of
 735 the upper ocean response to diurnal heating, cooling and wind mixing. *Journal of*
 736 *Geophysical Research*, 91, 8411–8427. <https://doi.org/10.1029/JC091iC07p08411>
- 737 Rembauville, M., Briggs, N., Ardyna, M., Uitz, J., Catala, P., Penkerch, C., ... Blain, S.
 738 (2017). Plankton Assemblage Estimated With BGC-Argo Floats in the Southern Ocean:
 739 Implications for Seasonal Successions and Particle Export. *Journal of Geophysical*
 740 *Research: Oceans*. <https://doi.org/10.1002/2017JC013067>
- 741 Roesler, C., Uitz, J., Claustre, H., Boss, E., Xing, X., Organelli, E., ... Barbieux, M. (2017).
 742 Recommendations for obtaining unbiased chlorophyll estimates from in situ chlorophyll
 743 fluorometers: A global analysis of WET Labs ECO sensors. *Limnology and*
 744 *Oceanography: Methods*, 15(6), 572–585. <https://doi.org/10.1002/lom3.10185>
- 745 Sanders, R., Henson, S. A., Koski, M., De La Rocha, C. L., Painter, S. C., Poulton, A. J., ...
 746 Martin, A. P. (2014). The Biological Carbon Pump in the North Atlantic. *Progress in*
 747 *Oceanography*, 129(PB), 200–218. <https://doi.org/10.1016/j.pocean.2014.05.005>
- 748 Schmechtig, C., Claustre, H., Poteau, A., & D'Ortenzio, F. (2014). Bio-Argo quality control
 749 manual for the Chlorophyll-A concentration. *Ifremer*, 13.
 750 <https://doi.org/http://dx.doi.org/10.13155/35385> Bio-Argo
- 751 Siegel, D. A., Buesseler, K. O., Behrenfeld, M. J., Benitez-Nelson, C. R., Boss, E.,
 752 Brzezinski, M. A., ... Steinberg, D. K. (2016). Prediction of the Export and Fate of
 753 Global Ocean Net Primary Production: The EXPORTS Science Plan. *Frontiers in*
 754 *Marine Science*, 3, 22. <https://doi.org/10.3389/fmars.2016.00022>
- 755 Smetacek, V. (1999). Diatoms and the ocean carbon cycle. *Protist News*, 150(1), 25–32.
 756 [https://doi.org/10.1016/S1434-4610\(99\)70006-4](https://doi.org/10.1016/S1434-4610(99)70006-4)
- 757 Smetacek, V. S. (1985). Role of sinking in diatom life-history cycles: ecological, evolutionary
 758 and geological significance. *Marine Biology*, 84(3), 239–251.
 759 <https://doi.org/10.1007/BF00392493>

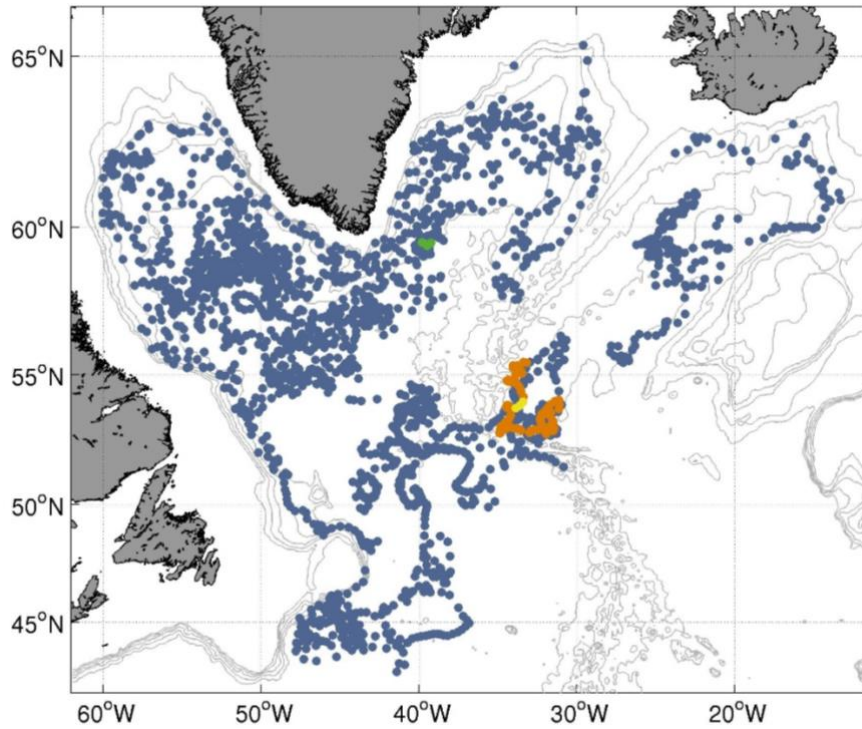
- 760 Steinberg, D. K., & Landry, M. R. (2017). Zooplankton and the Ocean Carbon Cycle. *Annual*
 761 *Review of Marine Science*, 9(1). <https://doi.org/10.1146/annurev-marine-010814-015924>
- 762 Steinberg, D. K., Van Mooy, B. A. S., Buesseler, K. O., Boyd, P. W., Kobari, T., & Karl, D.
 763 M. (2008). Bacterial vs. zooplankton control of sinking particle flux in the ocean's
 764 twilight zone. *Limnology and Oceanography*, 53(4), 1327–1338.
 765 <https://doi.org/10.4319/lo.2008.53.4.1327>
- 766 Stramski, D., Boss, E., Bogucki, D., & Voss, K. J. (2004). The role of seawater constituents in
 767 light backscattering in the ocean. *Progress in Oceanography*, 61(1), 27–56.
 768 <https://doi.org/10.1016/j.pocean.2004.07.001>
- 769 Stramski, D., Bricaud, A., & Morel, A. (2001). Modeling the inherent optical properties of the
 770 ocean based on the detailed composition of the planktonic community. *Applied Optics*,
 771 40(18), 2929–2945. <https://doi.org/10.1364/AO.40.002929>
- 772 Stramski, D., & Kiefer, D. A. (1991). Light scattering by microorganisms in the open ocean.
 773 *Progress in Oceanography*, 28(4), 343–383. [https://doi.org/10.1016/0079-](https://doi.org/10.1016/0079-6611(91)90032-H)
 774 [6611\(91\)90032-H](https://doi.org/10.1016/0079-6611(91)90032-H)
- 775 Taylor, J. R., & Ferrari, R. (2011). Shutdown of turbulent convection as a new criterion for
 776 the onset of spring phytoplankton blooms. *Limnol. Oceanogr.*, 56(6), 2293–2307.
- 777 Thomas, L. N., & Lee, C. M. (2005). Intensification of ocean fronts. *Bulletin of the American*
 778 *Meteorological Society*, 86(6), 783. <https://doi.org/10.1175/JPO2737.1>
- 779 Turner, J. T. (2002). Zooplankton fecal pellets, marine snow and sinking phytoplankton
 780 blooms. *Aquatic Microbial Ecology*, 27(1), 57–102. <https://doi.org/10.3354/ame027057>
- 781 Turner, J. T. (2004). The Importance of Small Pelagic Planktonic Copepods and Their Role in
 782 Pelagic Marine Food Webs. *Zoological Studies*, 43(2), 255–266.
- 783 Turner, J. T. (2015). Zooplankton fecal pellets, marine snow, phytodetritus and the ocean's
 784 biological pump. *Progress in Oceanography*, 130, 205–248.
 785 <https://doi.org/10.1016/j.pocean.2014.08.005>
- 786 Turner, J. T., Levinsen, H., Nielsen, T. G., & Hansen, B. W. (2001). Zooplankton feeding
 787 ecology: Grazing on phytoplankton and predation on protozoans by copepod and
 788 barnacle nauplii in Disko Bay, West Greenland. *Marine Ecology Progress Series*. Inter-
 789 Research Science Center. <https://doi.org/10.3354/meps221209>
- 790 Villa-Alfageme, M., de Soto, F. C., Ceballos-Romero, E., Giering, S., Le Moigne, F. A. C.,
 791 Henson, S., & Sanders, R. J. (2016). Geographical, seasonal and depth variation in
 792 sinking particle speeds in the North Atlantic. *Manuscript Submitted for Publication*.
 793 <https://doi.org/10.1002/2016GL069233>
- 794 Visser, A. W., Saito, H., Saiz, E., & Kjørboe, T. (2001). Observations of copepod feeding and
 795 vertical distribution under natural turbulent conditions in the North Sea. *Marine Biology*,
 796 138(5), 1011–1019. <https://doi.org/10.1007/s002270000520>
- 797 Wang, W., & Huang, R. X. (2004). Wind energy input to the surface waves. *Journal of*
 798 *Physical Oceanography*, 34(5), 1276–1280. [https://doi.org/10.1175/1520-](https://doi.org/10.1175/1520-0485(2004)034<1276:WEITTS>2.0.CO;2)
 799 [0485\(2004\)034<1276:WEITTS>2.0.CO;2](https://doi.org/10.1175/1520-0485(2004)034<1276:WEITTS>2.0.CO;2)
- 800 Wong, A., Keeley, R., Carval, T., & Argo Data Management Team. (2015). Argo Quality
 801 Control Manual For CTD and Trajectory Data, (December), 1–56. Retrieved from
 802 <http://archimer.ifremer.fr/doc/00228/33951/>
- 803 Woods, J. D. (1980). Diurnal and seasonal variation of convection in the wind-mixed layer of
 804 the ocean. *Quarterly Journal of the Royal Meteorological Society*, 106(449), 379–394.
 805 <https://doi.org/10.1002/qj.49710644902>
- 806 Woods, J. D., & Onken, R. (1982). Diurnal variation and primary production in the ocean
 807 preliminary results of a Lagrangian ensemble model. *Journal of Plankton Research*, 4(3),
 808 735–756. <https://doi.org/10.1093/plankt/4.3.735>
- 809 Xing, X., Briggs, N., Boss, E., & Claustre, H. (2018). Improved correction for non-

- 810 photochemical quenching of in situ chlorophyll fluorescence based on a synchronous
811 irradiance profile. *Opt. Express*, 26(19), 24734–24751.
812 <https://doi.org/10.1364/OE.26.024734>
- 813 Xing, X., Claustre, H., Boss, E., Roesler, C., Organelli, E., Poteau, A., ... D'Ortenzio, F.
814 (2017). Correction of profiles of in-situ chlorophyll fluorometry for the contribution of
815 fluorescence originating from non-algal matter. *Limnology and Oceanography: Methods*,
816 15(1), 80–93. <https://doi.org/10.1002/lom3.10144>
- 817 Xing, X., Morel, A., Claustre, H., Antoine, D., D'Ortenzio, F., Poteau, A., ... Hu, C. (2011).
818 Combined processing and mutual interpretation of radiometry and fluorimetry from
819 autonomous profiling Bio Argo floats: Chlorophyll a retrieval. *Journal of Geophysical*
820 *Research-Oceans*, 116(C6), C06020. <https://doi.org/10.1029/2010JC006899>
- 821 Zawada, D. G., Zaneveld, J. R. V., Boss, E., Gardner, W. D., Richardson, M. J., & Mishonov,
822 A. V. (2005). A comparison of hydrographically and optically derived mixed layer
823 depths. *Journal of Geophysical Research*, 110(C11), C11001.
824 <https://doi.org/10.1029/2004JC002417>
825
826



827
828

Figure 1. Schematic of the functioning of the intra-seasonal mixed layer pump.



829

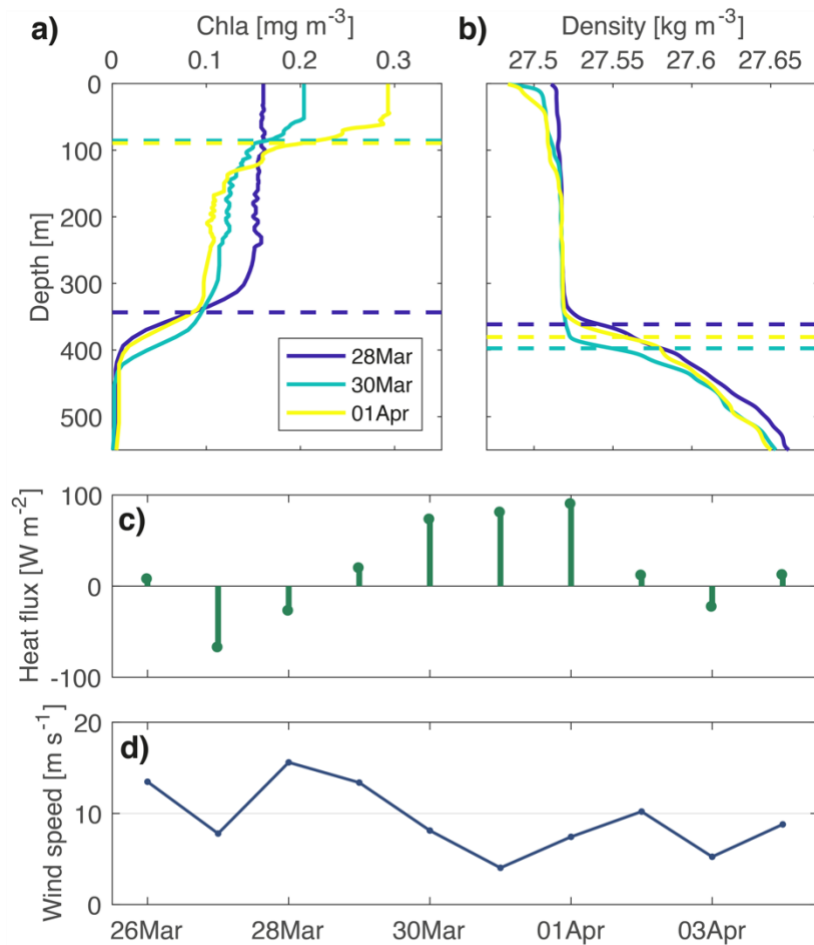
830

831

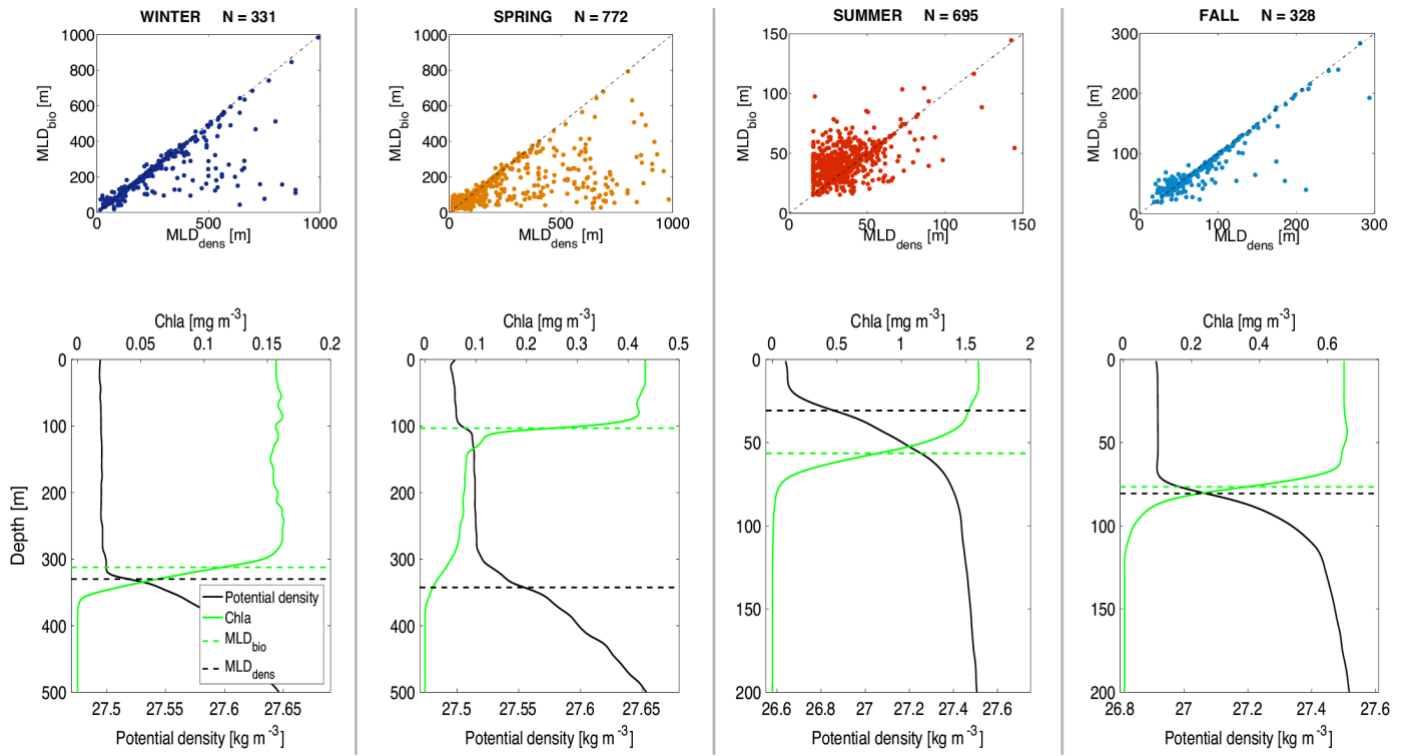
832

833

Figure 2. Location of the BGC-Argo float profiles in the subpolar North Atlantic Ocean during 2014-2016. Orange dots indicate the location of float 6901516 trajectory (January-December 2014) shown in Fig. 5. Yellow and green dots indicate the location of profiles shown in Fig. 7a and b respectively.

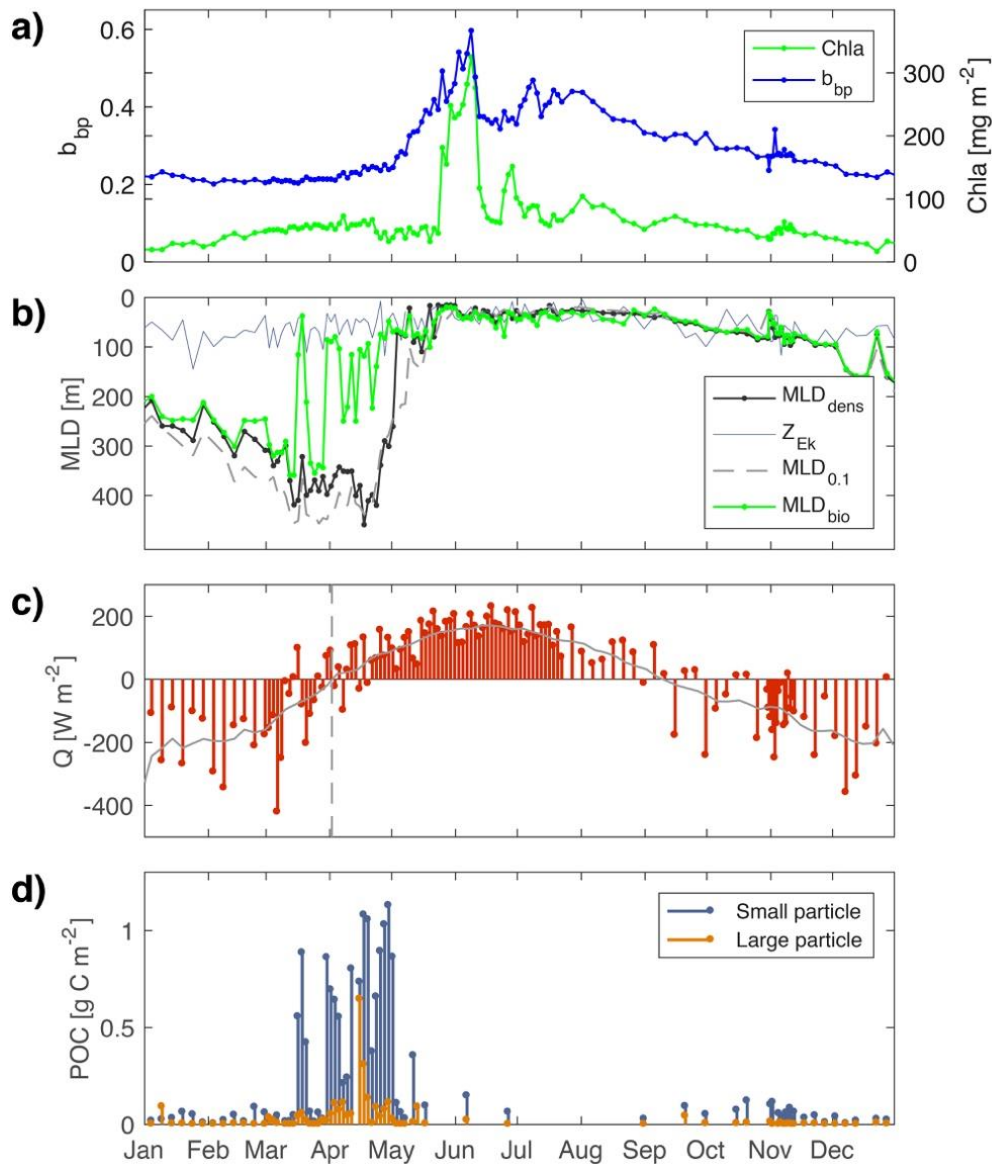


834
 835 **Figure 3.** Three BGC-Argo float profiles along the float 6901516 trajectory (yellow dots in Fig.
 836 2) sampled in the same water mass (see Fig. 7a) from March 28th to April 1st 2014. **a)** Chla
 837 profiles and **b)** density profiles with 2-day intervals. Horizontal dashed lines mark the depth of
 838 the maximum Chla gradient (MLD_{bio}) in **a)** and maximum density gradient (MLD_{dens}) in **b)**.
 839 Constant Chla in the upper layer in **a)** is due to NPQ correction. **c)** Daily net heat flux and **d)**
 840 wind speed along the float trajectory.



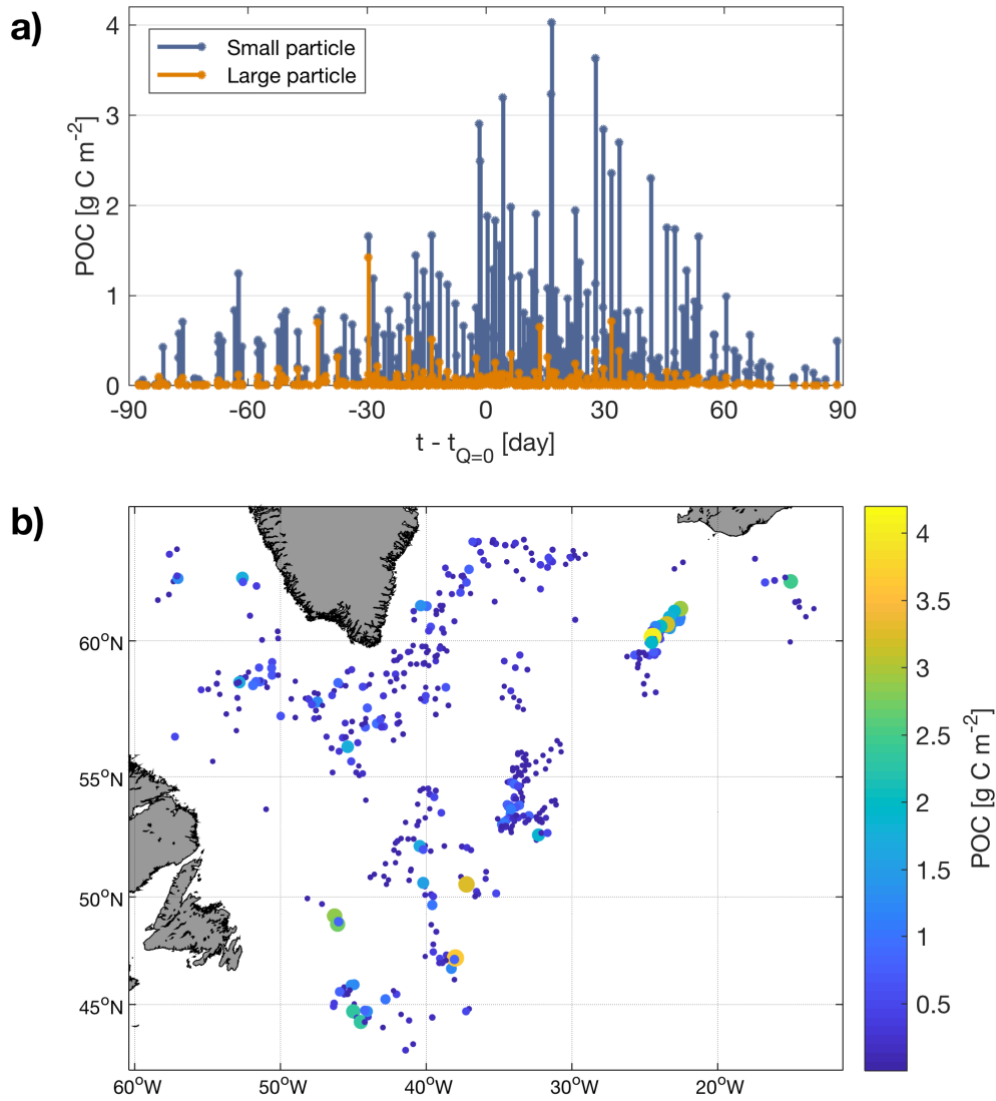
841

Figure 4. Seasonal difference between MLD_{bio} and MLD_{dens} for all the profiles shown in Fig. 2 (top) and examples of Chla and density profiles by season (bottom). Horizontal dashed black and green lines mark MLD_{dens} and MLD_{bio} respectively.



843
 844 **Figure 5.** Impact of the mixing layer dynamics on POC export. **a)** Chla and b_{bp} integrated over
 845 0-1,000 m depth (integrated b_{bp} is dimensionless), **b)** MLD_{dens} , MLD_{bio} , $MLD_{0.1}$ estimated with
 846 a density threshold of $0.1 \text{ kg}\cdot\text{m}^{-3}$, and the Ekman length scale Z_{Ek} , **c)** Daily-averaged net heat
 847 flux (Q) and **d)** POC stocks trapped in the remnant layer along the float 6901516 trajectory
 848 (January-December 2014). Continuous grey line and vertical dashed grey line in c) show 30-
 849 day smoothed net heat flux and the date of zero-crossing net heat flux respectively.

850



851

852 **Figure 6. a)** POC stock transferred to the mesopelagic by mixed layer pump events measured
 853 by the floats over the whole subpolar region. The time axis refers to the day of observation
 854 relative to the day where the sign of heat flux changes from negative to positive (see Fig. 5c).

855 **b)** Location of profiles presenting ML pump signature. Color and dot size denote the stock of
 856 small particles trapped in the remnant layer.

857

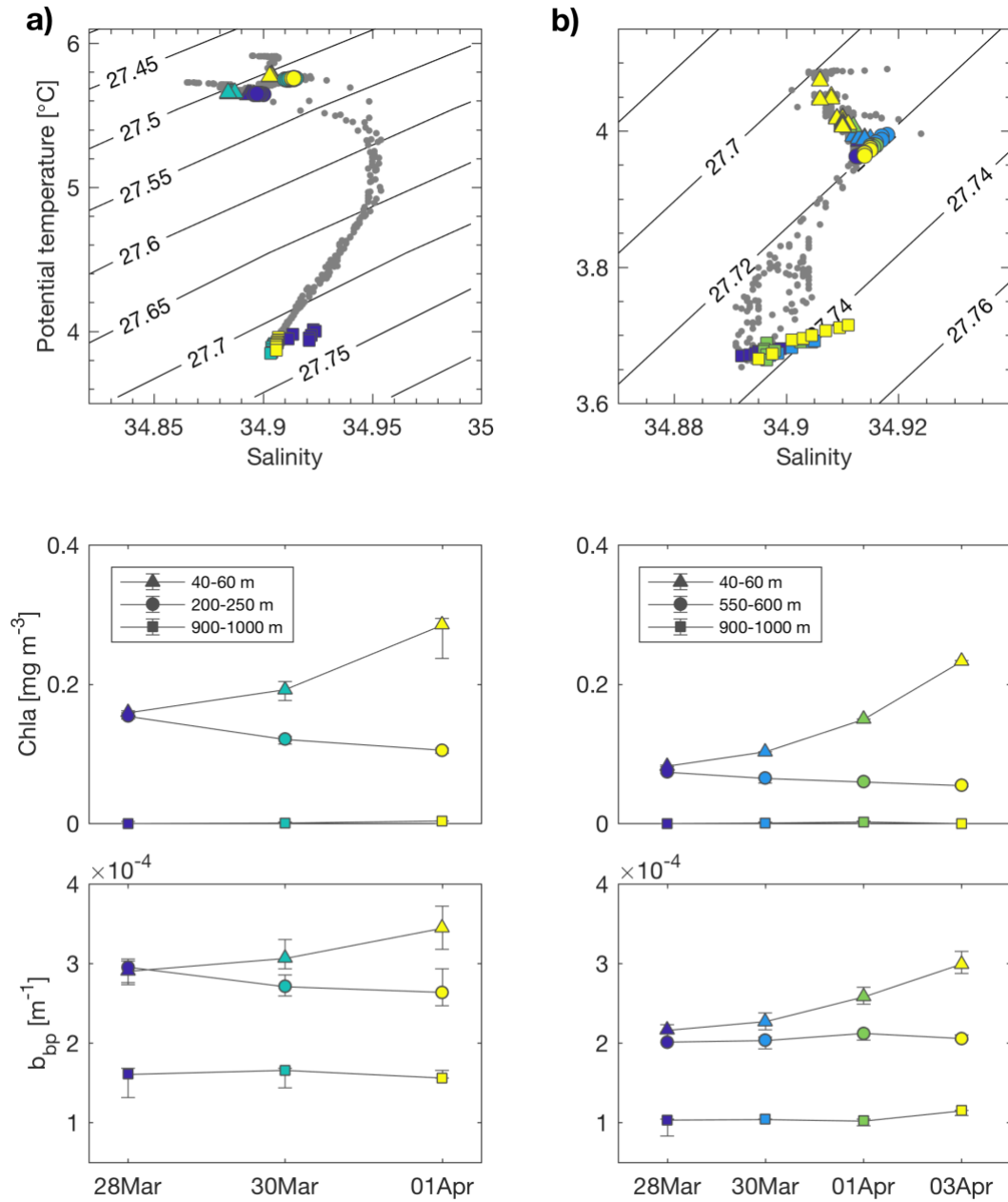
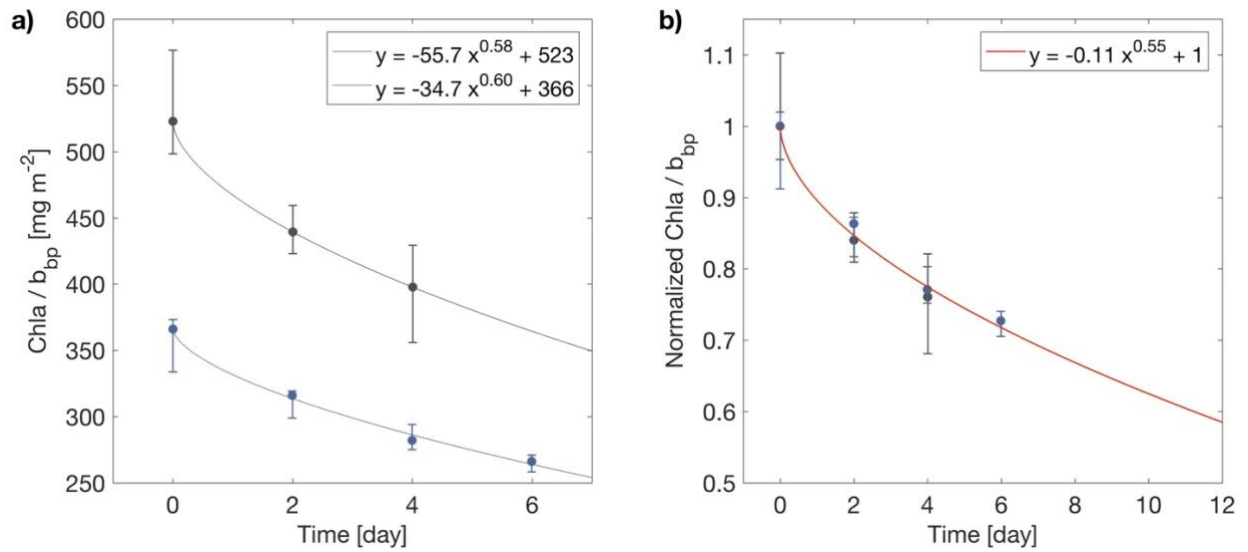
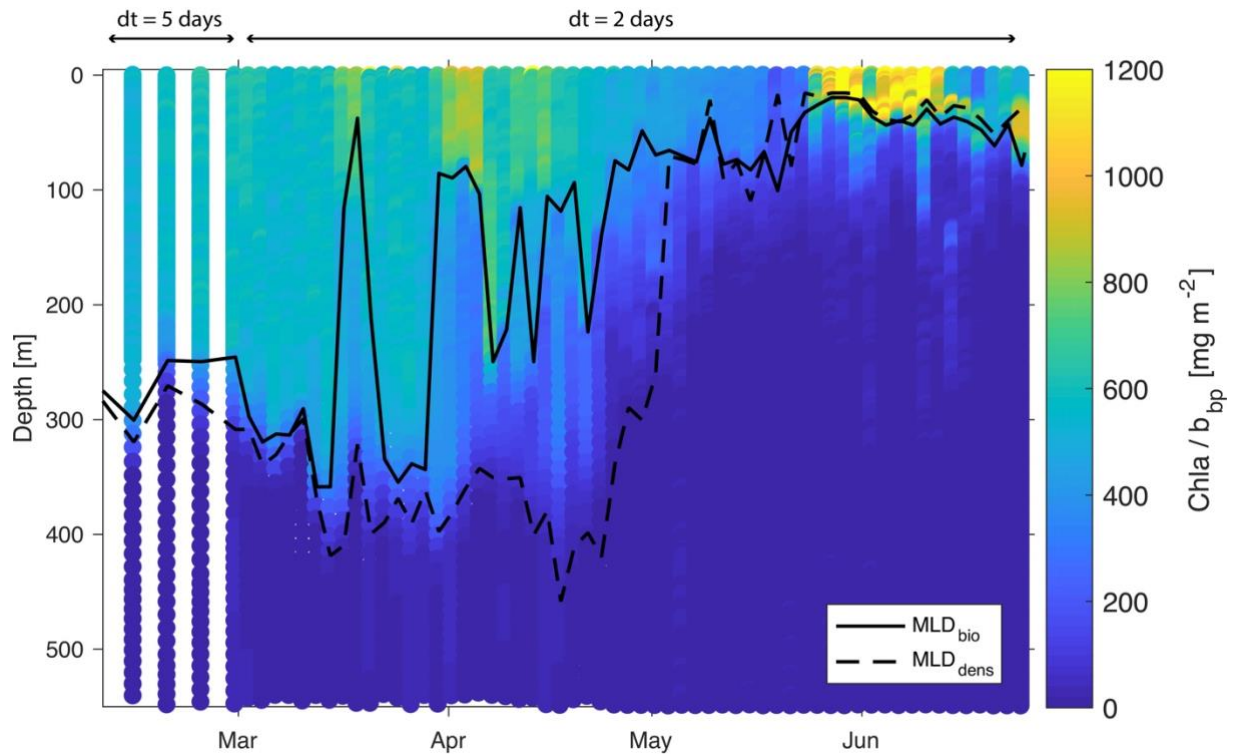


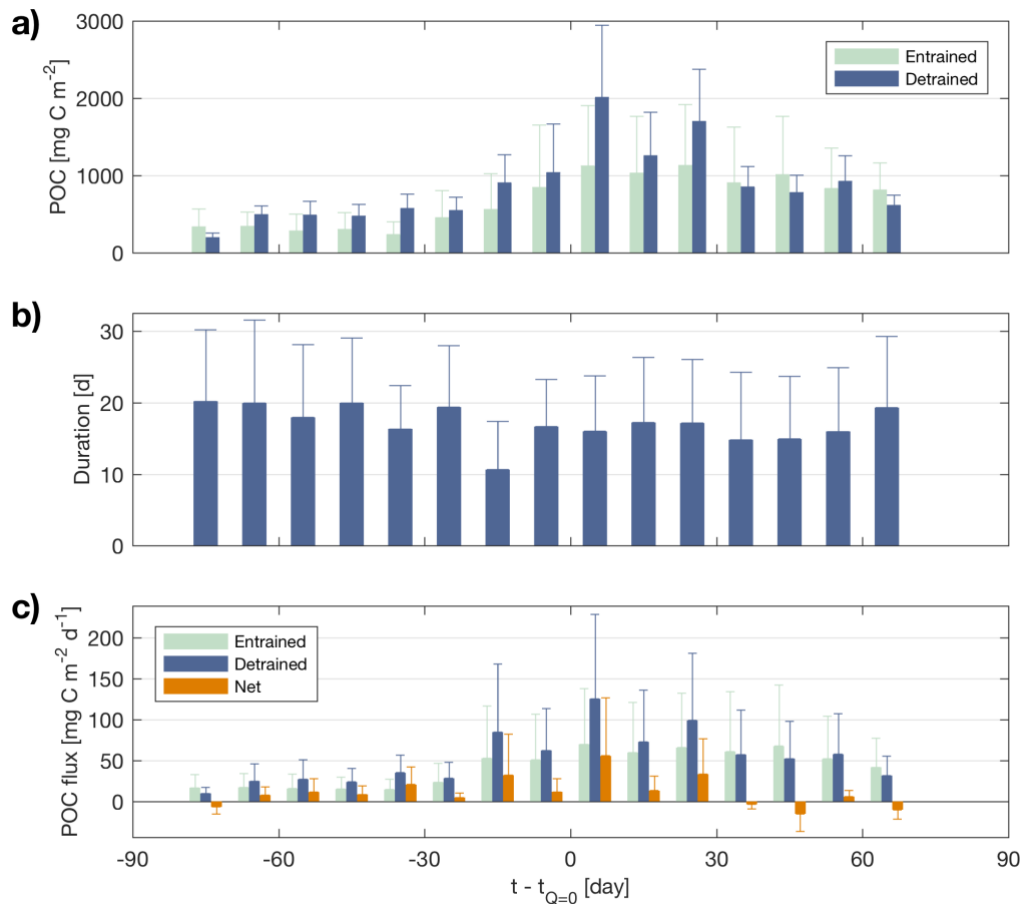
Figure 7. A quasi-Lagrangian approach to the ML pump. BGC-Argo float profiles along 2 sections of **a)** float 6901516 and **b)** float 6901480 acquired in 2014 (see location in Fig. 2). Top panels show potential temperature and salinity diagram for each profile of the 2 sections. Bottom panels show time evolution of mean Chla and b_{bp} from each profile over 3 different layers: surface (triangle), remnant (filled circle) and deep layer (square). Vertical error bars indicate the range of data points within each layer. Color of the symbols differentiates each profile.



861
 862 **Figure 8.** Time evolution of the Chla to b_{bp} ratio in the remnant layer. **a)** Absolute and **b)**
 863 normalized (by the maximum value) Chla to b_{bp} ratio for sections of float 6901516 (black line)
 864 and 6901480 (blue line) shown in Fig. 2 and 7. The red line represents the best-fit power law
 865 function for both float sections. The vertical error bars indicate the range of data points within
 866 the remnant layer.



867
 868 **Figure 9.** Time series of Chla to b_{bp} ratio at each depth along the float trajectory 6901516
 869 (February-July 2014). Solid black line and dashed black line represent MLD_{bio} and MLD_{dens}
 870 respectively. Time interval (dt) between successive profiles is indicated at the top of the panel.



871

872 **Figure 10.** a) POC stock entrained and detrained from the mixing layer, as estimated from
 873 initial conditions, b) duration of ML pump events (i.e. $2 < \Delta t >$) and c) Entrained, detrained
 874 and net ML pump-driven POC fluxes averaged over 10-day time periods in the whole subpolar
 875 North Atlantic Ocean. The length of error bars represents the average standard deviation of
 876 initial conditions associated to each ML pump signature detected within a 10-day time period.
 877 The time axis refers to the day of observation relative to the day where the sign of heat flux
 878 changes from negative to positive (see Fig. 5c).